Chem Soc Rev

Quantum dots derived from two-dimensional materials and their applications for catalysis and energy

Journal:	*Chemical Society Reviews*
Manuscript ID	CS-SYN-10-2015-000811.R2
Article Type:	Review Article
Date Submitted by the Author:	07-Jan-2016
Complete List of Authors:	wang, xuewan; NTU, Sun, Gengzhi; Nanyang Technological University Li, Nan; Nanyang Technological University, School of Chemical and Biomedical Engineering Chen, Peng; Nanyang Technological University, School of Chemical & Biomedical Engineering

Quantum dots derived from two-dimensional materials and their applications for catalysis and energy

Xuewan Wang, Gengzhi Sun, Nan Li and Peng Chen*

School of Chemical and Biomedical Engineering, Nanyang Technological University, 70 Nanyang Drive, 637457, Singapore

*correspondence to E-mail: ChenPeng@ntu.edu.sg

Abstract

Quantum dots (QDs) derived from the atomically-thin two-dimensional (2D) sheets (graphene, transition metal dichalcogenide, graphitic carbon nitride, hexagonal boron nitride, phosphorene) are emerging extraordinary zero-dimensional materials. Covering a broad spectrum of interesting optical, catalytic, electronic, chemical and electrochemical properties, these 2D-QDs promise a wide range of novel applications including imaging, sensing, cancer therapy, optoelectronics, display, catalysis, and energy. In this article, we discuss the synthesis methods and the properties of these 2D-QDs and emphasize their applications in electrocatalysis, photocatalysis, supercapacitor, batteries, and photovoltaics.

1 Introduction

In the past decade, graphene has created tremendous impacts in many fields.[1-3] Its success has triggered or reignited great interests on other two-dimensional (2D) nanomaterials, including hexagonal diatomic boron nitride (h-BN), graphitic carbon nitride (g-C_3N_4), transition metal dichalcogenides (TMDs, e.g. MoS_2, $MoSe_2$, WS_2, WSe_2), and monoatomic buckled crystals (e.g. black phosphorus atomic layer which is also known as phosphorene).[4-6] In the bulk forms, these materials are all characterized by strong covalent intralayer bonds and weak van der Waals interlayer interactions. Their atomically-thin 2D forms (single or few-layer) can hence stably exist and demonstrate distinct properties to their bulk counterparts. In spite of similar 2D structure, these materials cover a wide range of electronic, optical, catalytic, chemical, thermal, and magnetic properties, offering a rich arsenal for a plethora of applications.

When these 2D materials transform to 0D (i.e., lateral sizes being reduced to typically <20 nm), improved or new properties arise due to prominent edge and quantum confinement effects, and at the same time, some inherent merits of the 2D parents are still preserved. As compared with their native 2D forms, these new classes of 0D materials (quantum dots) offer even larger surface-to-volume ratio, better solubility in both aqueous and nonaqueous solvents, higher tunability in physiochemical properties, better amenability to hybridize with other nanomaterials, and more ease to be doped and functionalized. For instance, when 2D graphene sheet shrinks to 0D (graphene quantum dot – GQD), it starts to fluoresce. With the combination of several key merits (widely tunable photoluminescence properties, high chemical and photo stability, molecular size, nontoxicity, and high solubility), GQDs often outshine or complement conventional organic fluorophores and semiconductor quantum dots in bioimaging, optical sensing, and photovoltaics.[7-9] Other than serving as fluorophores, GQDs have also demonstrated unique advantages in other applications, particularly, in energy storage and conversion.[10, 11]

GQDs have added a new dimension to graphene research and stimulated the high expectation on the potentials of quantum dots derived from other 2D materials (2D-QDs). For example, it has been shown that MoS_2 edges have hydrogen absorption energy close to precious Pt-group metals and the catalytic activity of MoS_2 towards hydrogen evolution reaction (HER) is proportional to the number of edge sites.[12, 13] Therefore comparing to their 2D counterparts, MoS_2 QDs and WS_2 QDs are better HER electrocatalysts.[14] As another example, although g-C_3N_4 sheets are active towards oxygen reduction and water splitting, their applications are largely limited by its poor electrical conductivity. In comparison, g-C_3N_4 QDs have more abundant catalytically moieties (pyridinic N, graphitic N and edge amine groups) and can be easily hybridized with conducting nanomaterials for effective charge transfer.[15]

The research on quantum dots derived from 2D materials (2D-QDs) is at its infant stage. Their properties are still poorly understood and potentials are largely unexploited. Although several excellent review articles on synthesis, properties and applications of GQDs have been published in the recent years,[7, 10, 16-20] a comprehensive and comparative review on 2D-QD family is currently missing. In this article, the current synthesis methods are briefly reviewed and compared. Subsequently, we discuss the properties of these 2D-QDs and underscore their similarities and differences with the 2D counterparts and other 2D-QDs. With a wide range of extraordinary properties, 2D-QDs promise a huge variety of novel applications. Here, we place the emphasis on catalysis and energy applications and highlight their unique advantages over other nanomaterials.

2 Synthesis methods

A variety of synthetic routes have been devised to synthesize GQDs,[7] which can be well extended to prepare other 2D-QDs (Table 1). In general, 2D-QD synthesis methods fall into two broad groups: top-down and bottom-up approaches. As the properties of 2D-QDs are extremely sensitive to lateral size, thickness, edge configuration, chemical groups and dopants introduced during the synthesis, developing scalable and controllable synthesis methods is the key to the wide spread use of 2D-QDs.

Table 1 Synthetic routes for 2D-QDs

Methods	QDs	Precursors & treatment	Size (nm)	Height (nm)	Yield (wt%)	Ref.
Chemical etching	GQDs	carbon black, HNO_3 oxidation	15	< 0.7	44.5	21
	g-C_3N_4 QDs	bulk g-C_3N_4, H_2SO_4 treatment and DMF/H_2O hydrolysis	2~4	N/A	N/A	46
Hydrothermal / solvothermal methods	GQDs	GO sheets, hydrothermal in H_2O_2/$NH_3\cdot H_2O$	2.0 2.1 2.1	1.6 1.6 1.6	70 72 58	23
	GQDs	pyrene, nitration and hydrothermal in alkaline solution	2.6~3.8	1~2	45~63	52
	g-C_3N_4 QDs	bulk g-C_3N_4, H_2SO_4 / HNO_3 treatment, hydrothermal treatment in $NH_3\cdot H_2O$ and sonication	2~6	0.35	N/A	42
	h-BN QDs	bulk h-BN, sonication-solvothermal method	< 5	< 3	~30	29
	MoS_2 QDs WS_2 QDs	bulk MoS_2/WS_2, sonication assisted	3.3 2.5	1.2 1.2	13 18	14
	MoS_2 QDs	ammonia molybdate, thiourea, N-acetyl-L-cysteine	1.5~2.5	< 0.9	N/A	61
Electrochemical scissoring	GQDs	3D graphene electrode in ionic liquid	3	1.25	N/A	22
	MoS_2 QDs	bulk MoS_2 electrode in ionic liquid	2.5~6	0.8~1.5	N/A	41
	MoS_2 QDs	MoS_2 nanosheets, electro-Fenton reaction	3~8	< 2	N/A	40
Li/K intercalation	GQDs	MWCNT, K	18.5	0.9	23	24
	h-BN QDs	h-BN flake, K	10	0.9	2.1	27
	MoS_2 QDs	MoS_2 nanoparticles, Li	10~20	0.7	N/A	36
Ultrasonication	GQDs	graphene sheets, sonication in H_2SO_4/HNO_3	3~5	N/A	N/A	25
	$MoSe_2$ QDs	bulk $MoSe_2$, tip sonication with F-127	1.6~3	0.7~2.1	N/A	33
	Phosphorene QDs	black phosphorus powder, grinding and sonication	3.3~6.5	1~2.8	N/A	47

	Phosphorene QDs	black phosphorus powder, tip and bath sonication	0.8~4.4	0.9 ~2.1	N/A	49
Thermal/ microwave carbonization	GQDs	citric acid, 200 ºC for 30 min	4.2	1~2	N/A	54
	g-C_3N_4 QDs	thiourea and citric acid, 200 ºC for 2 h	2.78	N/A	N/A	60
	g-C_3N_4 QDs	Guanidine and EDTA, microwave (595 W, 12 s)	3.2~6.5	1.7	N/A	58

2.1 Top-down approaches

The raw 3D bulk materials or exfoliated 2D sheets can be broken down into 2D-QDs using chemical, electrochemical, or physical means. As comprehensively reviewed in several recent articles,[7, 18, 19] GQDs have been synthesized using chemical etching,[21] electrochemical scissoring,[22] hydrothermal/solvothermal cutting,[23] lithium/potassium intercalation,[24] ultrasonic treatment,[25] and ball-milling.[26] Some of these synthetic routes can be readily employed to make other types of 2D-QDs. For instance, single-layered h-BN QDs have been fabricated by a method previously used for high-yield production of GQDs, which involves potassium intercalation, subsequent de-intercalation *via* short exposure to air, and final exfoliation *via* reaction with ethanol-H_2O under ultrasonication.[24, 27] Sonication-assisted solvothermal technique has been applied for synthesis of h-BN QDs.[28, 29] It has been found that temperature, filling factor, and reaction time exert significant influence on the size distribution and surface chemistry of h-BN QDs. Because of the weak van der Waals force between TMD layers, ultrasonication, sometimes with assistance of grinding or solvothermal treatment, can be used to conveniently obtain TMD-QDs (e.g. MoS_2, WS_2, ReS_2, TaS_2, $MoSe_2$, WSe_2 and $NbSe_2$ QDs).[14, 30-34] Li or K intercalation method has also been used to produce WS_2 and MoS_2 QDs taking advantage of the large interlayer distance of these TMD materials (d = 0.615~ 0.618 nm, much larger than that of graphite).[35-37] Alkali metal intercalation can only be conducted in air and water free conditions. Alternatively, H_2SO_4 or Na^+ ion intercalation can be used to synthesize MoS_2 or WS_2 QDs in ambient and aqueous conditions.[38, 39] Like for GQDs, electrochemical etching in ionic liquid and electrochemically induced Fenton reaction have also been found to be efficient for mass-production of MoS_2 QDs.[40, 41] As compared with other 2D materials, g-C_3N_4 has relatively stronger interlayer interaction because of hydrogen bonding between polymeric melon units with NH/NH_2 groups.[42] Chemical etching (strong acids or a mixture of ammonia and hydrogen peroxide) and hydrothermal treatments are more effective to exfoliate g-C_3N_4 QDs.[42-46] Considering the air- and water-sensitive nature of phosphorene QDs, a combination of grinding and sonication under inert gas protection is utilized for their synthesis.[47, 48] Recently, highly-oxidized phosphorene QDs have been synthesized under ambient condition *via* ultrasonciation.[49]

2.2 Bottom-up approaches

2D-QDs can be chemically assembled by smaller building blocks or transformed from precursors of comparable sizes. GQDs have been precisely synthesized using stepwise organic synthesis, albeit with low-throughput and difficulty to prevent aggregation caused by strong pi-pi interaction.[50, 51] But similar realization may not be possible for other 2D-QDs. GQDs can also be produced by pyrolysis / carbonization or hydrothermal / solvothermal reaction of small organic molecules.[52-54] In such processes, heteroatoms may be inherited from the precursor molecules thus conveniently achieving interesting doping effects.[55, 56] For example, N-doped GQDs have been synthesized under hydrothermal conditions with citric acid as carbon source and urea / hexamethylene tetraamine / diethylene amine / ethanol-amine / ethylene diamine as nitrogen source.[56] The N-doping concentration and fluorescence quantum yield (QY) largely depends on the chosen N-precursor. As another example, hydrothermal treatment of fructose in the presence of sulphuric acid produced monodispersed crystalline S-doped GQDs.[57]

Although also made of carbon and nitrogen, the structural and physiochemical properties of g-C_3N_4 QDs are significantly different to N-doped GQDs. By a microwave pyrolysis approach, g-C_3N_4 QDs with a high QY of 35% were synthesized with guanidine hydrochloride and ethylenediaminetetraacetic acid as the precursors.[58] Synthesis of QDs and compositing with other functional nanomaterials can be simultaneously attained. Using CH_2N_2, $Bi(NO_3)_5$ and NaH_2PO_4 as the precursors, Li *et al.* prepared g-C_3N_4 QDs/$BiPO_4$ nanocrystals composite by combining sonochemical and thermal annealing processes.[59] Conceivably, g-C_3N_4 QDs are thermally grown from CH_2N_2 molecules adsorbed on surface of $BiPO_4$ nanocrystals. Lu *et al.* have reported a solid-phase thermal treatment (200 °C, 4h) of citric acid and thiourea mixture to produce oxygen (O) and sulfur (S) co-doped g-C_3N_4 QDs with narrow size distribution.[60]

Huang *et al.* synthesized water-soluble MoS_2 QDs by a facile, one-pot hydrothermal approach, wherein ammonium molybdate and thiourea were used as molybdenum and sulfur precursors, respectively.[61] N-acetyl-L-cysteine was added as the capping agent to confine the hydrothermal growth of monolayer MoS_2 QDs. The resultant MoS_2 QDs are uniform in size (~90.7% in the range of 1.5-2.5 nm) and single-layered (thickness < 0.9 nm). Using sodium molybdate and L-cysteine as the precursors, Wang *et al.* prepared MoS_2 QDs (average thickness ~1.79 nm) by a similar hydrothermal route.[62] Ren *et al.* hydrothermally synthesized monolayer MoS_2 QDs with an average size of 3.6 nm using sodium molybdate and dibenzyl disulfides as the molybdenum and sulfur source, respectively.[63] MoS_2 QDs have also been made by a colloidal solvothermal route using ammonium tetrathiomolybdate as the precursor and oleylamine as the reducing and stabilizing agent.[64] The size of MoS_2 QDs (2~7 nm) can be tuned by controlling the amount of olelamine and reaction time. MoS_2 QDs-graphene-TiO_2 composite has been synthesized by a simple one-pot solvothermal approach, wherein sodium molybdate, thiocarbamide, TiO_2 powder were reacted with graphene oxide (GO) dispersion in dimethylacetamide/H_2O mixed solvent.[65] It should be aware that solvents used in solution chemistry based syntheses may block the active sites of QDs.

3 Properties

The family of 2D materials covers a wide range of physicochemical properties. For example, their electronic characteristics vary from semi-metallic (graphene) to insulating (h-BN) (Fig. 1).[66] Being sensitive to size-dependent quantum confinement, edge configurations, defects, chemical functionalities, and heteroatom dopants, the property range of 2D-QDs is further extended in terms of, e.g., light adsorption and emission profile and mechanism, catalytic activities, electrochemical characteristics.

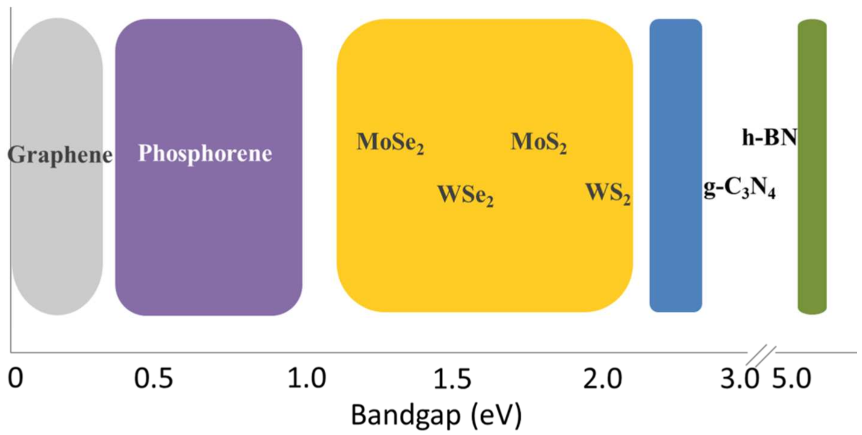

Fig. 1 Band structures of 2D crystalline materials. Adapted and modified with permission from ref. 66. Copyright (2014) Nature Publishing Group.

3.1 Graphene quantum dots (GQDs)

GQDs are single or few layered graphene with lateral size typically <20 nm, which often bear defects in graphitic lattice, chemical moieties, and heteroatom dopants (Fig. 2a). In contrast to zero-bandgap semimetallic 2D pristine graphene sheet, GQDs are fluorescent and semiconductive with size-dependent bandgap due to quantum confinement. With diameter varying from 0.46 to 2.31 nm, pristine GQDs emit from UV (bandgap of 6.81 eV) to infrared (bandgap of 1.64 eV) (Fig. 2b).[67] In addition to the prominent size-dependence, the photoluminescence (PL) properties of GQDs can also be sensitively modulated by chemical groups, heteroatom dopants, defects, geometry, and edge configurations. The PL properties are intriguingly governed by the combination or competition between intrinsic and defect state emission. The former derives from quantum confinement, edge effects (zigzag or armchair edge), and radiative recombination of localized electron-hole pairs, while the latter is induced by energy trap states because of chemical groups, dopants or vacancy defects. The high tunability makes it challenging to synthesize GQDs with homogeneous properties. On the other hand, it also endows GQDs a wide range of interesting properties. For example, heteroatom doping is able to enhance fluorescence quantum yield[56, 68] and confer interesting upconversion properties on GQDs attributable to anti-Stokes transition or multiphoton active process.[69-71]

As compared with the conventional organic fluorophores and widely used semiconductor quantum dots, GQDs are superior for various applications owing to its unique combination of several key merits, including wide coverage of emission wavelength, high photostability, molecular size, good dissolvability in both aqueous and organic solvents, ease to be covalently or non-covalently conjugated with a wide range of molecules, and high chemical inertness.

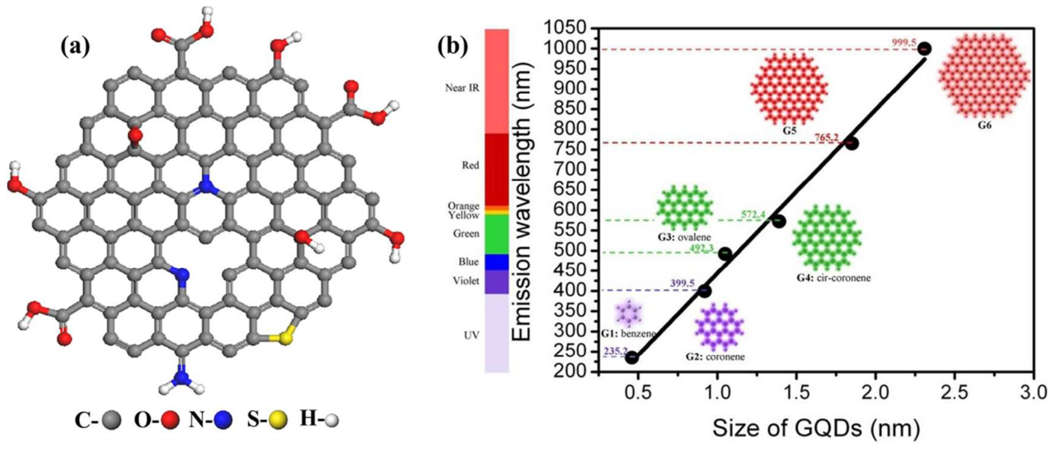

Fig. 2 (a) Schematic of heteroatom doped GQDs. (b) Calculated emission wavelength (nm) as a function of the diameter of GQDs. (b) adapted and modified with permission from ref. 67. Copyright (2014) Royal Society of Chemistry.

In the UV-vis absorption spectrum of GQDs, two characteristic absorption peaks are often observed, specifically, a peak between 200 – 270 nm due to π–π* transition and another peak between 270 – 390 nm due to n–π* transition from C=O functional groups introduced during the synthesis processes.[10, 18] GQDs with other functional groups can extend their adsorption from UV to visible region. For example, a single crystalline amine-functionalized GQD exhibits an additional excitonic absorption peaks between 400 – 500 nm.[52] This GQD offers a large molar extinction coefficient of ~ 10^6 M^{-1} cm^{-1} within the visible region, which is larger than the semiconductor QDs and other widely used light absorbers in solar cells (e.g., ruthenium complexes). GQDs with upconversion properties are able to absorb NIR.[72]

The possible wide-range absorption and emission profile of GQDs makes them attractive for designing efficient solar cells and photocatalysis systems. It has been reported that GQDs have two orders of magnitude slower hot carrier cooling rate (100~300 ps) than that in bulk graphene, and significantly less fast hot carrier relaxation pathways (e.g. surface trap states) than that in semiconductor QDs (e.g. CdSe, PbSe), thereby enabling more efficient hot charge carrier harvesting in solar energy conversion.[73] TiO_2 is widely used as photocatalyst and light-harvesting inorganic semiconductor. But it can only utilize UV light (a small fraction of energy contained in solar light) due to its wide bandgap and it is also blamed for its low photocatalytic activity because of the fast charge recombination rate. GQDs can serve as sensitizer to significantly extend the absorption range of TiO_2.[25] In addition, both theoretical and experimental evidence suggests that chemical bonding between the oxygen functional groups of GQD and TiO_2 enables ultrafast hot electron injection from photoexcited GQDs to the conduction band of TiO_2 (< 15 fs, much faster than its electron-hole recombination rate of >80 fs).[74, 75] It means that GQDs can significantly enhance the hot charge carrier capture capability of TiO_2.

It has been shown that GQDs are multivalent redox species with discrete single-electron transfer behavior.[76] Electron transfer between the different oxidation states of GQDs may endow them with interesting electrochemical and catalytic properties. The edge sites, chemical groups, defects, and heteroatom dopants on GQDs dictate the electrochemical and catalytic properties of GQDs.[2, 7, 10] Interestingly, GQDs with oxygenated groups exhibit high peroxidase-like activity.[77] Taking advantage of their ability to catalyze the decomposition of H_2O_2 to hydroxyl radical ($^{\cdot}OH$), GQDs have been utilized to improve wound disinfection.[78] Experimental and theoretical studies have shown that -C=O groups and O=C-O groups on GQDs serve as the catalytically active sites and H_2O_2 binding sites, respectively.[79]

Because of their low oxidation potential (0.48 V) and strong electrostatic interaction with positively charged ions, graphene oxide (GO) sheets are effective reducing agents for precious metal ions which has higher reduction potentials (e.g., 1.5 V for Au^{3+}).[80, 81] GQDs which usually bear oxygenated groups or other functionalities shall have the same or even better ability in this regard because of smaller size as well as higher fraction of edge sites and functional moieties. Chemical groups with electron donating or withdrawing groups, vacancy defects, and heteroatom dopants can modulate the redox potentials of GQDs (thus its catalytic properties) and act as active sites (e.g. to promote anchoring and nucleation of metal nanoparticles).[81-83] Photoexcited GQDs exhibit excellent electron donating capability, therefore facilitating fast reduction of metal ions and subsequent formation of metal nanoparticles (NPs). For example, N-doped GQDs have been used as efficient photocatalysts for photochemical synthesis of Ag NPs onto g-C_3N_4.[84]

Co-doping of p-type and n-type heteroatoms on a GQD may lead to the formation of photochemical diodes which are desired for the separation of photogenerated charges. Such co-doped GQDs have been found to be useful as photocatalysts for water splitting.[85] GQDs may act as co-catalysts instead. For instance, it has been shown that the defects on GQDs is able to enhance the catalytic activities of Pt NPs for oxygen reduction by promoting charge transfer from the NPs, dissociative adsorption of oxygen molecules, and binding of reaction intermediates on the metal surface.[86]

3.2 Graphitic carbon nitride (g-C_3N_4) QDs

Atomic sheet of g-C_3N_4 can be regarded as N-substituted graphene framework. Although sharing similar 2D structure and delocalized π-conjugated electronic structure, g-C_3N_4 sheet and graphene sheet differ significantly in physicochemical properties and so do their QD forms. g-C_3N_4 sheet is composed of tri-s-triazine units bridged by amino groups, with periodic vacancies in their lattices (Fig. 3a).[87] Such "poly(tri-s-triazine)" framework is highly defective and disorder in nature. The abundant graphitic or pyridinic N atoms in sp^2 plane and amine groups (–NH or –NH_2) on the terminating edges may give rise to interesting catalytic and other properties.

According to DFT calculations, the bandgap of an infinite g-C_3N_4 sheet is 2.1 eV and it opens to 3.5 eV in tri-s-triazine molecule (the smallest g-C_3N_4 QD).[87] And g-C_3N_4 QD bears a high percentage of amine edges as well as oxygenated groups inevitably introduced in the synthesis (Fig. 3b).[46, 88] The strong quantum confinement in g-C_3N_4 QDs causes blue shift in UV-vis and PL spectra.[44, 46] Similar to GQDs, the UV-vis absorption spectrum of g-C_3N_4 QDs gives two characteristic peaks due to π–π^* transition of s-triazine rings and n-π^* transition of carbonyl groups with the adsorption tail extending to the visible region.[58, 60, 89] Despite the existence of amine groups, the synthesized g-C_3N_4 QDs are negatively charged because of introduced oxygenated groups.[43, 58, 89]

g-C_3N_4 QDs (~4.5 nm in size) synthesized by a low-temperature solid-phase method emit bright blue fluorescence with a high QY of 42%.[89] Remarkably different from the g-C_3N_4 QDs synthesized using other methods, g-C_3N_4 QDs (~3 nm) obtained from hydrolysis of bulk g-C_3N_4 in acidic solution emit excitation-independent UV light (peaking at 367 nm) with a high QY of 46% (Figure 3c and d).[46] The authors proposed that the electronic transition of aromatic sp^2 C-N (i.e., from n nonbonding orbital of nitrogen atom to π antibonding orbital of sp^2-carbon) dictates the PL properties of these QDs instead of their hydroxyl and amine groups (Figure 3c). Upconversion PL phenomena on the basis of the multiphoton active process have been observed in g-C_3N_4 QDs.[42] Single-layered g-C_3N_4 QDs has been theoretically and experimentally shown to have two-photon upconversion property (adsorption of two near-infrared photons leads to emission of green PL) due to π–π* charge-transfer.[45] It is speculated that, similar to GQDs, the adsorption and emission profiles of g-C_3N_4 QDs can be widely tuned by size, chemical modification, and heteroatom doping. For example, blue shift may be caused by sulfur doping and red shift may be resulted from boron or fluoride doping.[90] It has been shown that heteroatom dopant (S) can be inherited from the precursor molecule during thermal annealing.[60]

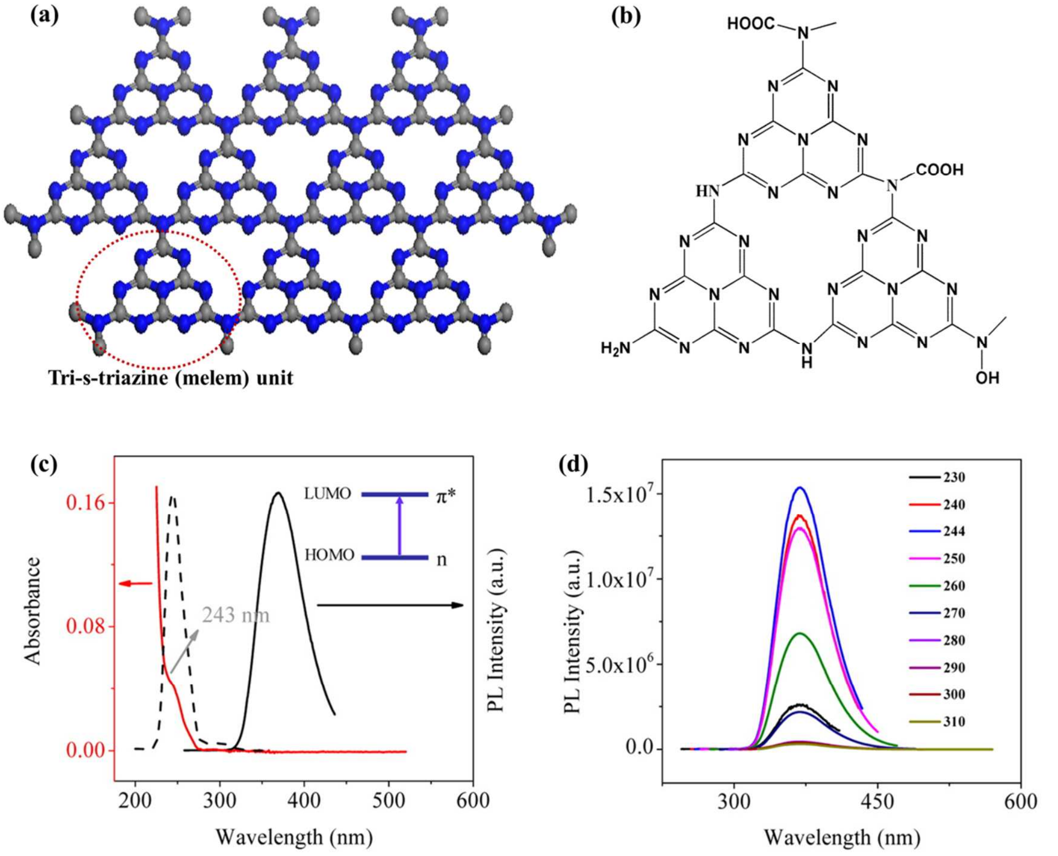

Fig. 3 Schematics of (a) g-C_3N_4 sheet and (b) g-C_3N_4 QD with 3 tri-s-triazine unites and chemical functionalities. (c) UV-vis absorption (red), PL excitation (dashed line), and PL emission (solid line) of g-C_3N_4 QDs synthesized *via* hydrolysis of bulk g-C_3N_4 in DMF and H_2SO_4 mixture solution. (d) PL spectra of g-C_3N_4 QDs at different excitation wavelengths. (c and d) adapted with permission from ref. 46. Copyright (2015) American Chemical Society.

g-C_3N_4 sheet has rich surface moieties that are catalytically active, such as pyridinic and graphitic N, Bronsted basic functionalities, and H-bonding amine groups.[91] It has been identified as a promising metal-free electrocatalyst or photocatalyst for hydrogen evolution reaction (HER), oxygen evolution reaction (OER) and oxygen reduction reaction (ORR).[92] g-C_3N_4 is superior to TiO_2 (the commonly used photocatalyst) for HER and OER in the sense that the water oxidation and reduction potentials are better engulfed by its valence band and conduction band.[90] Wang *et al.* reported that g-C_3N_4 is capable of photo-splitting water in neutral, acidic or basic conditions.[87, 93] Theoretical calculations showed that N atoms in g-C_3N_4 are the preferable oxidation sites for H_2O to O_2 conversion, whereas C atoms provide the reduction sites for H^+ to H_2 conversion.[87] g-C_3N_4 QDs, which have more enriched catalytic sites, higher quantum yield, larger specific surface area, prominent quantum and edge effects, are expected to outperform bulk g-C_3N_4 in photocatalysis and electrocatalysis.

3.3 Hexagonal boron nitride (h-BN) QDs

2D h-BN sheet may be depicted as a graphene layer with C atoms fully substituted by alternating B and N atoms (Fig. 4a). In the honeycomb arrangement, covalently bonded B-N is isostructural and isoelectroinc like C-C in graphene. Therefore unsurprisingly, h-BN sheet has almost identical lattice parameters as graphene sheet, and comparable in-plane mechanical strength and thermal conductivity. Also similar to graphene, h-BN layer is attractive for its exceptional chemical and thermal stability. On the other hand, in contrast to C-C bond, the covalent B-N bond also exhibits ionic characteristics due to the electronegativity difference between B and N atoms. This makes the electronic, magnetic and chemical properties of h-BN significantly differ from that of graphene. For example, h-BN sheet is an insulator or wide-gap (5.0–6.0 eV) semiconductor in contrast to zero-gap semi-metallic graphene.

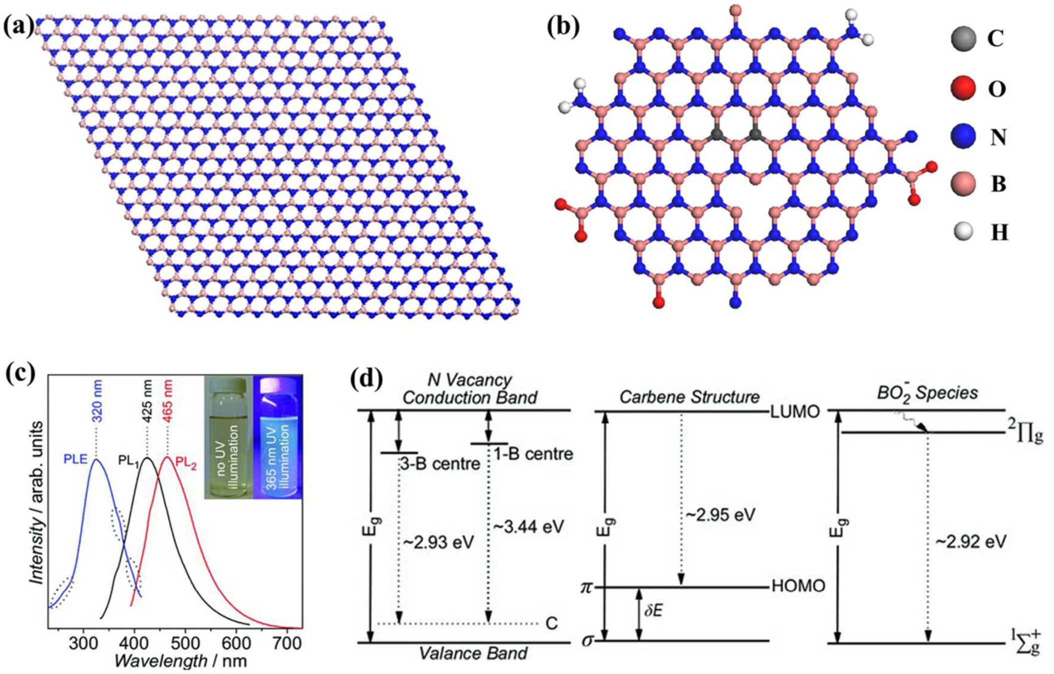

Fig. 4 (a) Schematic of h-BN. (b) Schematic of C-doped h-BN QD. (c) PL-excitation and PL spectra of synthesized h-BN QDs (insets are the photographs of h-BN QDs with and without UV illumination). (d) Luminescence diagrams of different luminescent centers of h-BN QDs. (c and d) adapted with permission from ref. 27. Copyright (2014) Wiley Publishing Group.

New properties arise in h-BN QDs, the low-dimensional siblings of h-BN sheets (Fig. 4b). Like GQDs, the electronic, magnetic and optical properties of h-BN QDs are highly tunable by shape, size, doping, and edge sites.[94-96] Edge hydrogenation thermal-dynamically stabilizes h-BN QDs and significantly diminishes their magnetic ground states caused by spin polarization of unpaired electrons on edges.[96] In contrast to GQDs, h-BN QDs with fully hydrogenated edges are spin-unpolarized and have a bandgap of ~4.85 eV which is not sensitive to QD size. Edge hydroxylation of h-BN QDs is even more energetically favorable and causes more reduction in electronic bandgap.[94] As h-BN QD is the hybrid of two elements, the variation of its edge configurations is much richer than that of GQDs.

Carbon, neighboring element to both B and N, is an energetically favored dopant to h-BN QDs. The B–C–N networks, a ternary semiconductor, with adjustable B, C and N content and arrangements are able to offer rich composition and structure dependent electronic, magnetic and surface properties.[97, 98] It has been theoretically shown that C atom energetically prefers to replace the minority element (B or N) in the inner region of h-BN QD.[99] A h-BN QD has a larger HOMO-LUMO gap than a GQD of the same size,[100] and C doping (more significant at edge sites) decreases the bandgap of h-BN QD thereby extending the absorption wavelength from UV to the visible spectrum.[95, 99]

Bandyopadhyay *et al.* theoretically investigated the effects of charge transfer on the properties of h-BN QDs and GQDs using tetracyanoquinodimethane and tetrathiafulvalene as the molecular dopants.[100] Unlike GQDs, h-BN QDs can only weakly interact with these dopants because h-BN lacks of π surface for strong π-π interaction. Despite the weak interaction, the bandgap of h-BN QDs (4.03 eV) can however be reduced by more than 50% after physisorption of the molecular dopants. According to theoretical calculations, external electric field is also capable of dramatically reducing (even fully closing) HOMO-LUMO gap of h-BN QDs.[94]

Monolayered h-BN QDs (lateral size ~10 nm) have been exfoliated and disintegrated from h-BN flakes.[27] The chemical composition of the resultant h-BN QDs are characterized to be $BNC_{0.12}O_{0.21}$ with the existence of N-B-O, O-B-O and C-N/C-B species. The C dopants are likely obtained from the solvent used. This h-BN QD, with a wide direct bandgap of 6.51 eV, shows strong UV absorption (<350 nm) and weak blue fluorescence (QY ~2.5%) probably arisen from carbon-replaced N vacancy point defects, carbene structure at zigzag edges and BO_x^- (x = 1 and 2) species (Fig. 4c and d). The PL lifetimes from these three luminescent centers are all in nanoseconds, which is an advantageous feature for optoelectronic and bio-imaging applications. Blue PL emission (maximum at 442 nm) is also observed from the h-BN QDs (diameter ~3.3 nm and thickness ~2.5 nm) prepared by a sonication-assisted solvothermal approach at 140 ºC.[28] The size, surface chemistry and hence optical properties of h-BN QDs can be controllably tailored by adjusting solvothermal conditions. h-BN QDs (~3.46 nm) solvothermally prepared at 200 ºC, filling factor of 67% and reaction time of 24 h exhibit excitation-dependent PL emission (peaking at 395.5 nm) with a high QY of 19.5%.[29] Stengl *et al.* synthesized poly-dispersed h-BN and BCN QDs (< 40 nm) by solvothermal refluxing BN and BCN sheets, which exhibit strong blue luminescence.[101]

3.4 Transition metal dichalcogenide (TMD) QDs

A single-layered TMD (formulated as X-M-X) is a plane of transition metal atoms (M) covalently sandwiched by two hexagonal planes of chalcogen atoms (X). Unlike graphene, layered TMDs are non-centrosymmetric. To obtain QDs, it is necessary to break the intra-plane X-M-X bonds and consequently abundant edge atoms (M and X) are produced (Fig. 5a). Theoretical calculations showed that monolayer MoS_2 QDs are metallic because of the coordinative-unsaturated Mo atoms at the edges.[102] Contradictorily, experimentally synthesized TMD QDs are found to be dominantly 2H phase in their crystal structure, indicating the semiconductive nature.[14, 30, 35, 40] Such discrepancy can be attributed to the passivation of metal dangling bonds (e.g. forming metal oxide or hydroxide)[14, 31] or to the fact that the TMD-QDs are mostly terminated by chalcogen atoms instead of metal atoms.[35, 40] In comparison with their 2D sheets, the bandgaps of TMD QDs open up due to quantum confining effects. For example, WS_2 QDs (8~15 nm in size) synthesized by Lin *et al.* exhibit a larger direct bandgap of 3.16 eV compared to that of their bulk sheets (2.1 eV).[35] Similarly shown in another study, MoS_2 QDs with lateral size of ~2.1 nm has a widened direct bandgap of 3.96 eV compared to that of monolayered 2D sheets (1.89 eV).[61] In addition to the size-dependent quantum confinement, bandgap is also strongly influenced by defects, functional groups, dopants, *etc.* introduced in the synthesis. This explains why a larger monolayer MoS_2 QD (~3.6 nm) has a higher bandgap of 4.96 eV.[63]

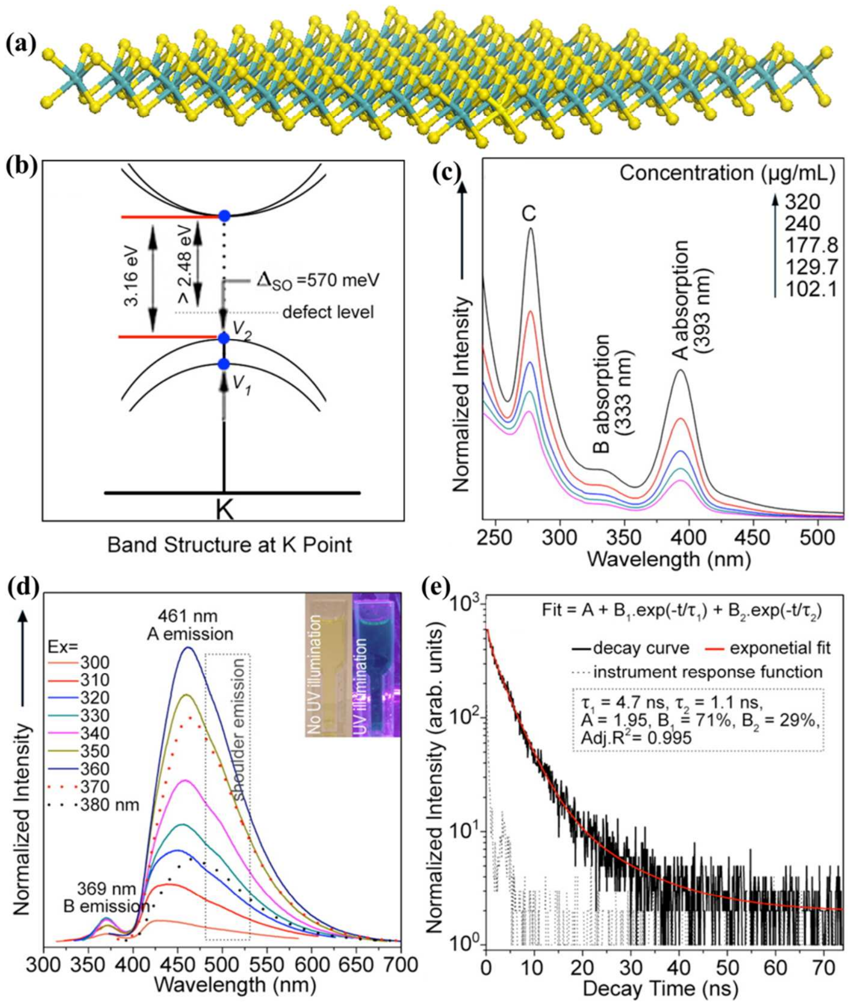

Fig. 5 (a) Schematic of WS_2 QD. (b – e) Diagram of the band structure, UV-vis absorption spectra, PL spectra and time resolved PL decay profile (emission at 461 nm and excitation at 360 nm) of WS_2 QDs. Inset of (d) is the photograph of WS_2 QDs with and without UV illumination. (b-e) Adapted and modified with permission from ref. 35. Copyright (2013) American Chemical Society.

Inversion symmetry is absent in monolayered TMD sheets, leading to novel spin-valley coupled band structures. As compared to 2D WS_2 sheets, a significantly enhanced spin-valley coupling has been observed from WS_2 QDs (570 *vs.* 400 meV) (Fig. 5b).[35] This is evidenced by the broadening of excitonic absorption peak A (393 nm)-B (333 nm) splitting in the UV-vis spectra, wherein peak A and B are generated by the direct bandgap transition at K point with energy split from valence band spin-orbit coupling (Fig. 5c). In UV-vis spectra, another characteristic absorption peak C (~277 nm) can also be observed, which is due to the optical transition between the density of state peaks in the valence and conductance bands. Because of large spin-valley coupling WS_2 QDs demonstrate multiple PL emission peaks in the blue-green region with lifetimes in nanosecond scale (Fig. 5d and e).[35] Compared with WS_2 sheets, the QDs have blue-shift in the UV-vis absorption and PL emission, as well as improved QY (~4%).

Similarly, MoS_2 QDs synthesized from an one-pot hydrothermal method using N-acetyl-L-cysteine (NAC) as the capping agent exhibit a large spin-valley coupling of 700 meV and characteristic absorption peak A at 380 nm, peak B at 313 nm and peak C at 264 nm.[61] With excitation at 380 nm, multiple PL emission peaks (strongest at 480 nm, QY ~ 2%) are observed. Interestingly, NAC-capped MoS_2 QDs show unusual upconversion PL with strongest emission also at 480 nm under excitation wavelength of 780 nm. The origin of upconversion may be attributed to the energy transfer from NIR absorption by the NAC shell to the MoS_2 QD core.[61] Just like other 2D-QDs, the impurities introduced during the synthetic routes and the QD size have strong influences on the properties of TMD QDs. The monolayered MoS_2 QDs synthesized by a combination of sonication and solvothermal treatment on MoS_2 powders give only one prominent UV absorption peak and an excitation-dependent PL behavior.[14] MoS_2 QDs (both 2H and 1T phases) prepared by Li intercalation and exfoliation of MoS_2 nanoparticles have an excitation-independent PL peak at 415 nm.[36] It has been demonstrated that ion intercalation in an alkaline environment can significantly increase the QY of the MoS_2 QDs (4.84% at excitation of 440 nm) prepared *via* ultrasonication of MoS_2 powder.[39] Interestingly, the MoS_2-ZnS hybrid QD possesses two PL emission centers (at 380 and 450 nm).[103] Owing to the size-dependent bandgap opening, the colloidal MoS_2 QDs obtained from a bottom-up solvothermal method emit from blue (430 nm) to red (600 nm) while increasing the size from 2 to 7 nm.[64] Gan *et al.* synthesized MoS_2 QDs *via* ultrasonic exfoliation and found that both the photoluminescence excitation (PLE) peak position and absorption band edge red-shift with increasing particle diameter.[32]

Gopalakrishnan *et al.* electrochemically etched MoS_2 QDs from bulk MoS_2 in ionic liquid solutions.[41] To explain a peculiar observation that size reduction leads to red-shift in PL emission, they proposed that the surface trap states resulting from the uncompensated sulfide ions and metal ions increase with the increasing surface-to-volume ratio (or decreasing size). MoS_2 QDs exfoliated from their parental sheets *via* electro-Fenton reaction exhibit a strong pH-dependent PL behavior, *i.e.*, strong emission under alkaline condition and being almost completely quenched under acidic condition.[40] The transformation of semiconducting MoS_2 (2H) QDs to the metallic MoS_2 (1T) QDs caused by H^+ intercalation may be responsible for the PL quenching. In comparison, the PL of NAC-capped MoS_2 QDs is pH insensitive, suggesting that intrinsic state emission is dominating and defect state emission is suppressed by NAC.[61] WS_2 QDs recently fabricated by combining physical grinding, H_2SO_4 intercalation and ultrasonication show strong UV and NIR absorption (increasing with decreasing QD size).[38] Such NIR harvesting ability confers WS_2 QDs (~3 nm) a high photothermal conversion efficiency of 44.3% at 808 nm. Similarly, $MoSe_2$ QDs (2~3 nm) prepared by tip-ultrasonication has an extinction coefficient of 17.4 $Lg^{-1}cm^{-1}$ and a photothermal conversion efficiency of 46.5% measured at 785 nm.[33] Distinct to other 2D-QDs, these $MoSe_2$ QDs have no PL emission.

TMD-based nanomaterials (e.g., MoS_2 and WS_2 nanosheets) have interesting electrocatalytic properties. For example, nanoparticulate MoS_2 is a promising precious-metal-free nanocatalyst for hydrogen evolution reaction (HER) because its hydrogen binding energy is close to that of platinum-group metals.[12] The electrocatalytic performance of MoS_2 toward HER (overpotential, current density and Tafel slope) can be improved with the increase of active edge sites and decrease of particle size.[12] Wang *et al.* found that small MoS_2 QDs (~2 nm) demonstrate better HER and ORR performance than larger MoS_2 particles.[13] Electronic structure calculation and the partial charge analysis suggested that MoS_2 QDs with armchair edges may have better catalytic ability than those with zigzag edges.[104]

MoS_2 sheets are effective for charge storage because they allow easy intercalation of foreign ions (e.g. H^+, Li^+, Na^+ and K^+),[105, 106] and exhibit pseudo-capacitance behavior because Mo can transit between different valence states (+2 to +6).[105, 107] For MoS_2 QDs, ion intercalation is even easier. Other TMD QDs (specifically, ReS_2, TaS_2, WSe_2 and $NbSe_2$ QDs) have been successfully prepared by a combination of a grinding and sonication process.[30] But their optical, catalytic, electrochemical properties have not yet been characterized.

3.5 Atomic black phosphorus (phosphorene) QDs

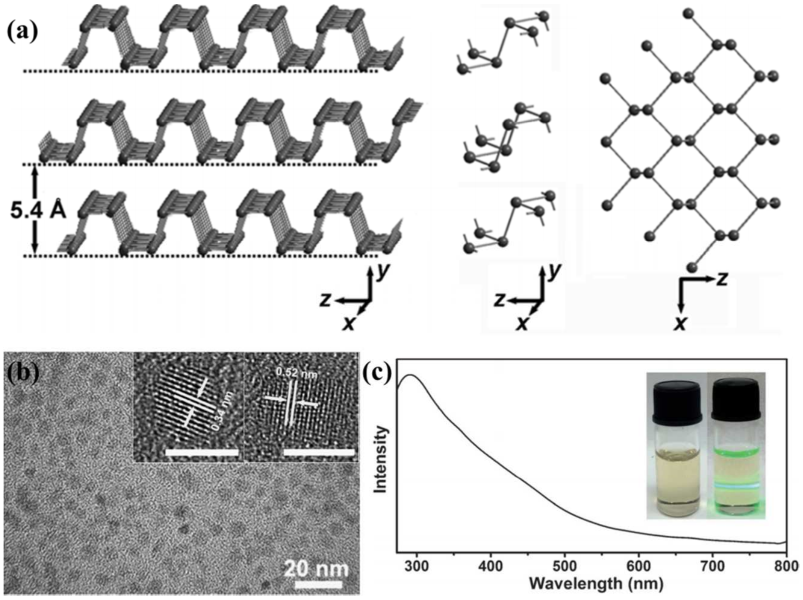

Fig. 6 (a) Schematic of bulk black phosphorus. (b) TEM images of phosphorene QDs. Inset: HRTEM images of phosphorene with different lattice fringes. (c) UV-vis absorption spectrum of phosphorene QDs. Inset: photos of the phosphorene QDs and their Tyndall effect. Adapted with permission from ref. 47. Copyright (2015) Wiley Publishing Group.

Phosphorene is an atomically-thin layer of black phosphorous (BP) crystal (Fig. 5a), in which each phosphorus (P) atom is covalently bonded with three others forming a puckered honeycomb structure.[47] Free-standing monolayered phosphorene is a semiconductor with an inherent direct bandgap theoretically predicted to be 0.8~1.5 eV, which fills the gap between graphene and dichalcogenides (Fig. 1).[66, 108] The charge-carrier mobility of few-layer quasi-2D phosphorene is measured up to 1000 cm^2 V^{-1} s^{-1} at room temperature.[109] The relatively small direct bandgap and high mobility make phosphorene desirable in many applications in optoelectronics and energy.[108-111] Phosphorene QDs (diameter ~4.9 nm and thickness ~1.9 nm) have been produced from BP powders *via* sonication, which can be stably dispersed in N-methyl-2-pyrrolidone (Fig. 5b).[47] Their absorption profile well-extends to the visible light region (absorption edge >700 nm) (Fig. 5c). Despite being the least reactive allotrope of phosphorus, phosphorene and its QDs are sensitive to water and air. Such susceptibility imposes challenges to synthesize, characterize, and apply pristine phosphorene QDs. But pristine phosphorene QDs can be used in the energy devices which operate in the conditions free of water and oxygen, such as, lithium or sodium ion batteries.

And on the other hand, oxidation provides the opportunity to tailor the electronic and optical properties of phosphorene QDs for different application purposes. For example, oxidized phosphorene QDs have better water solubility and NIR adsorption, which are desirable, e.g., for photothermal therapy.[49] Wang *et al.* theoretically predicted the stable existence of 2D phosphorene oxide, an analogue to graphene oxide.[112] However, the synthesis and understanding of their properties have yet to be demonstrated.

4 Catalysis applications

4.1 Electrocatalysis

4.1.1 Oxygen reduction reaction (ORR)

The cathodic ORR is the rate-limiting factor for fuel cells and metal-air batteries. Heteroatom doping can transform graphene sheets to state-of-the-art noble-metal-free electrocatalysts for ORR. Doping effects are usually more prominent in 0D GQDs. Li *et al.* demonstrated that N-doped GQDs (N/C atomic ratio of *ca.* 4.3%, synthesized by a facile electrochemical etching approach) have the desired four-electron transfer pathway in ORR and remarkable methanol tolerance.[113] A theoretical study proposed that pyridinic and graphitic N dopants on GQD are the most active sites for ORR.[114] Favaro *et al.* showed that co-doping of electron-rich N and electron-poor B on GQD can produce synergistic effects to improve ORR performance.[115] Furthermore, removal of oxygen functional groups by simple chemical reduction can change the catalytic activity of N,B co-doped GQDs from a two-electron pathway to the ideal four-electron pathway.

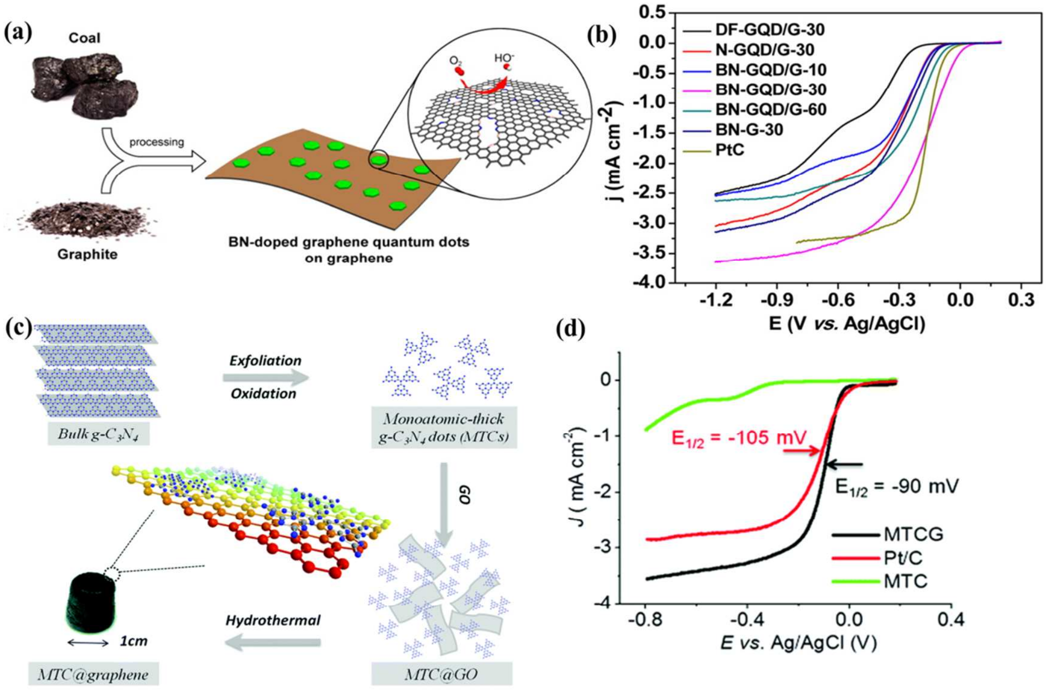

Fig. 7 (a and b) Illustration of fabrication procedure for B,N co-doped GQD/rGO composite and the ORR polarization curves at a scan rate of 5 mV s^{-1} and rotating speed of 900 rpm in O_2 saturated 0.1 KOH solution. Adapted with permission from ref. 117. Copyright (2014) American Chemical Society. (c and d) Synthetic protocol of g-C_3N_4 QDs/rGO composite and the ORR polarization curves at a scan rate of 10 mV s^{-1} and rotating speed of 1200 rpm in O_2 saturated 0.1 KOH solution. Adapted with permission from ref. 15. Copyright (2015) Royal Society of Chemistry.

Through the strong π-π interaction, GQDs can readily be hybridized with other graphene materials (pristine graphene, graphene oxide – GO, reduced graphene oxide – rGO, graphene nanoribbon, 3D graphene foam, *etc.*). Good ORR performance with positively shifted onset and peak potential has been obtained from N,S co-doped rGO/GQD hybrid (with N/C=4.74% and S/C=1.76%).[116] The charge polarization and spin density induced by N and S dopants synergistically improve ORR performance. B,N co-doped rGO/GQD hybrid (13.6 at% B and 18.3 at% N) prepared from coal and graphite has been reported as an excellent electrocatalyst for ORR, which gives more positive onset potential, higher diffusion-limited current density and larger kinetic current density than commercial Pt/C catalysts (Fig. 7a and b).[117] The inferior performance of bare B,N co-doped rGO suggests the pivotal roles of doped GQDs.

Because of their small sizes and attached functional groups, GQDs may be easily composited with other nanomaterials. For example, PtCu@GQDs capsules obtained by a simultaneous reduction and assembly strategy offer a 110 mV more positive onset potential and 1.3 times higher mass activity than that of bare PtCu capsules.[118] GQD decorated Pt nanoparticles (NPs) which are solvothermally synthesized provide a 70 mV more positive onset potential, a 9 times higher current density, and much improved stability as compared to commercial Pt/C catalysts.[119] It is believed that the defective GQDs facilitate the binding of oxygen molecule and its intermediates on the surface of Pt NPs.

g-C_3N_4 QDs are also promising catalysts for ORR due to high content of pyridinic and graphitic N, large surface area and abundant edge amine sites. However, their poor intrinsic conductivity is the major obstacle for electrocatalytic applications. Considering the excellent electrical conductivity of graphene and its structural similarity with g-C_3N_4, Wang *et al.* prepared g-C_3N_4 QDs/rGO composite as the efficient catalyst for ORR (Fig. 7c).[15] The homogeneous and intimate interaction between g-C_3N_4 QDs and graphene produced a catalyst rivaling performance of the commercial Pt/C catalyst in terms of catalytic current density and half-wave potential (Fig. 7d).

h-BN is not able to act as an electrocatalyst because it is an insulator with a wide bandgap and is chemically inert.[120] But heteroatom or molecular dopants may endow h-BN with electrocatalytic properties. A theoretical study suggests that nitrogen doped h-BN (lattice B atoms substituted by N atoms) has catalytic activity towards ORR and the adsorption energy of O_2, O, OH, OOH, and H_2O on its surface is similar to that on Pt(111) surface.[121]

Using a simple two-step drop-casting process, Wang *et al.* coated MoS_2 QDs (≤ 2 nm) on a gold nanoparticle (AuNP) film.[122] Such electrode demonstrates a direct four-electron ORR pathway with large limiting current density and small onset overpotential, comparable to a commercial Pt/C catalyst modified electrode. The enhanced performance takes the advantages of the small onset overpotential of AuNP film and promoted second oxygen reduction step by MoS_2 QDs. The composite outperforms the commercial Pt/C catalysts in terms of long term stability and methanol tolerance. Du *et al.* confined hydrothermally synthesized MoS_2 QDs in 3D porous N-doped graphene as effective ORR catalysts.[123] Well-exposed active sites of MoS_2 QDs and good conductivity of 3D graphene enable a prominent positive shift in both onset potential (to 0.95 V) and peak potential (to 0.82 V), and a four-electron-transfer pathway with an even higher current density than the commercial Pt/C catalysts.

4.1.2 Hydrogen evolution reaction (HER)

Producing clean fuel by water electrolysis (i.e., hydrogen evolution reaction) is a promising solution for both energy and environment crises. Ren *et al.* employed hydrothermally synthesized MoS_2 QDs as HER electrocatalysts, with an onset overpotential of ~160 mV, Tafel slope of 59 mV dec^{-1}, and ~14 times more current density than the bulk MoS_2 powders at the overpotential of 400 mV.[63] The enhanced performance of MoS_2 QDs could be ascribed to the abundant active edge sites and faster electron transfer between QDs because of low interlayer potential barrier between these monolayer structures. Gopalakrishnan *et al.* prepared a heterodimensional catalyst system by interspersing MoS_2 QDs in few-layered MoS_2 sheets *via* a liquid exfoliation technique.[31] It shows a good HER activity with an onset overpotential of ~190 mV, a Tafel slope of ~ 74 mV dec^{-1} and a large exchange current density of 3.2 $x10^{-5}$ A cm^{-2}. Similarly, Xu and coworkers prepared QD / nanosheet composite of MoS_2 or WS_2 by a sonication and solvothermal process (Fig. 8a).[14] The obtained heterodimensional catalyst system based on MoS_2 (or WS_2) gives an onset overpotential of ~120 mV (or ~180 mV), much smaller than that of the nanosheets based systems (>350 mV) (Fig. 8b). The MoS_2 (or WS_2) based heterodimensional catalyst also exhibits a smaller Tafel slope of 69 ~ 75 mV dec^{-1} than that of commercially available MoS_2 (115 mV dec^{-1}) or WS_2 (138 mV dec^{-1}) catalysts (Fig. 8c). In addition, the MoS_2 based catalyst is remarkably stable as evidenced by the almost identical polarization curves before and after 2000 cycles. The improvement brought by incorporation of MoS_2 and WS_2 QDs is due to the facts that the electrocatalytic activity is linearly correlated with the number of edge sites,[12] and QDs carry rich edge sites. Qiao *et al.* recently exfoliated differently-sized MoS_2 nanosheets from bulk MoS_2 using repetitive Li intercalation process.[37] HER tests showed that monolayer MoS_2 QDs (diameter 2~10 nm) are much superior to MoS_2 nanosheets (lateral size 100~800 nm), in terms of a much lower onset potential (120 *vs.* 371 mV), smaller Tafel slope (69 *vs.* 181 mV per decade), larger exchange current density (17.9 *vs.* 3.9 $\mu A\ cm^{-2}$) and higher turnover frequency (0.048 *vs.* 0.010 s^{-1}). This study clearly demonstrates the advantages of TMD QDs over their 2D sheets for electrocatalysis.

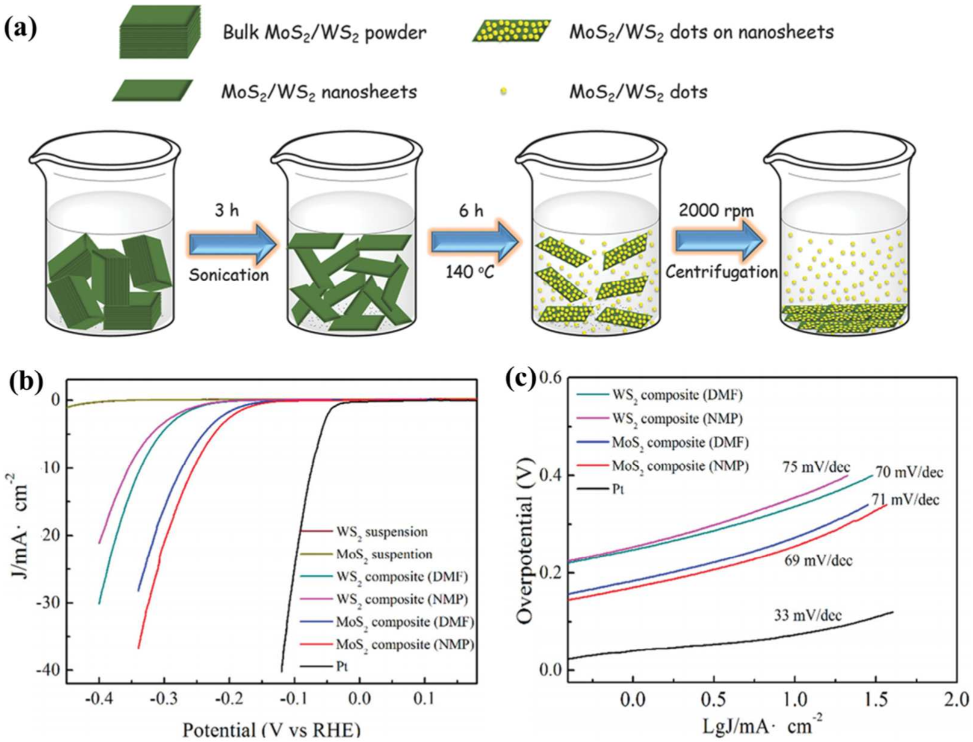

Fig. 8 (a) Synthesis of heterodimensional catalyst system consisting MoS_2 (or WS_2) QDs and MoS_2 (or WS_2) nanosheets. (b) HER polarization curves and (c) Tafel plots of the QD / nanosheet composite of MoS_2 or WS_2. Adapted with permission from ref. 14. Copyright (2015) Wiley Publishing Group.

Metal-free 2D-QDs (GQDs, h-BN QDs, g-C_3N_4 QDs, phosphorene QDs) have largely unexplored as HER catalysts. Qiao's group found that coupling g-C_3N_4 with N-doped graphene leads to highly active HER catalysts, wherein the former provides active sites for hydrogen adsorption and the latter facilitates the electron transfer for proton reduction.[124] This study suggests the potential of g-C_3N_4 QDs. Sim *et al.* prepared N-doped GQDs by nitrogen plasma treatment of CVD-grown graphene sheets.[125] Glassy carbon electrode (GCE) modified with these N-doped GQDs exhibits an onset HER potential of -0.22 V in 1 M perchloric acid solution, positively shifted by 0.1 V relative to that of pristine graphene. Moreover, a Tafel slope of 45 mV per decade and an exchange current density of 7.1×10^{-5} A cm^{-2} have been obtained, which are far superior to that of pristine graphene.

4.2 Photocatalysis

Semiconductor QDs have been widely used as narrow-bandgap sensitizers to harvest solar energy.

However, these traditional QDs (such as, CdX: X=S, Se, Te and PbS) usually suffer from many surface traps, which hinder efficient charge separation and transfer. In addition, they degrade over time due to reaction with some electrolytes or because of photo-oxidation under prolonged illumination. And semiconductor QDs made of heavy metals are toxic and thus environmentally hazardous.

2D-QDs are attractive alternatives for photocatalysis because of their excellent photochemical robustness, low-toxicity, unique and tunable optical and catalytic properties. Using GQDs with upconversion properties, Zhuo *et al.* designed TiO_2/GQD complex photocatalyst which is able to harness the visible spectrum of sunlight.[25] 97% degradation of methylene blue (MB) under 1h visible light illumination indicates the high photocatalytic activity of rutile TiO_2/GQDs. Pan *et al.* prepared GQD-sensitized TiO_2 nanotube-arrays (GQD-TNAs) as a heterojunction photoelectrocatalyst. Under visible light, its photoelectrocatalytic (PEC) activity is 5.7 times larger than bare TNA and its efficiency towards MB degradation is 2 times higher than CdS QD sensitized TNA.[126] Moreover, GQD-TNAs are much superior to CdS/CdSe QD-TNAs in terms of cycling stability. Li *et al.* synthesized g-C_3N_4 QD/$BiPO_4$ as a visible light-induced photocatalyst for methyl orange (MO) degradation, which can achieve an efficiency of 92% within 3h (much better than 75% efficiency with g-C_3N_4 powder) (Fig. 9a).[59] Because the conduction band and valence band of g-C_3N_4 QDs are more negative than those of $BiPO_4$, the separation and transport of photo-generated electron-hole pairs are enhanced at the interface. In addition, g-C_3N_4 QDs give much larger specific surface area than its powder form.

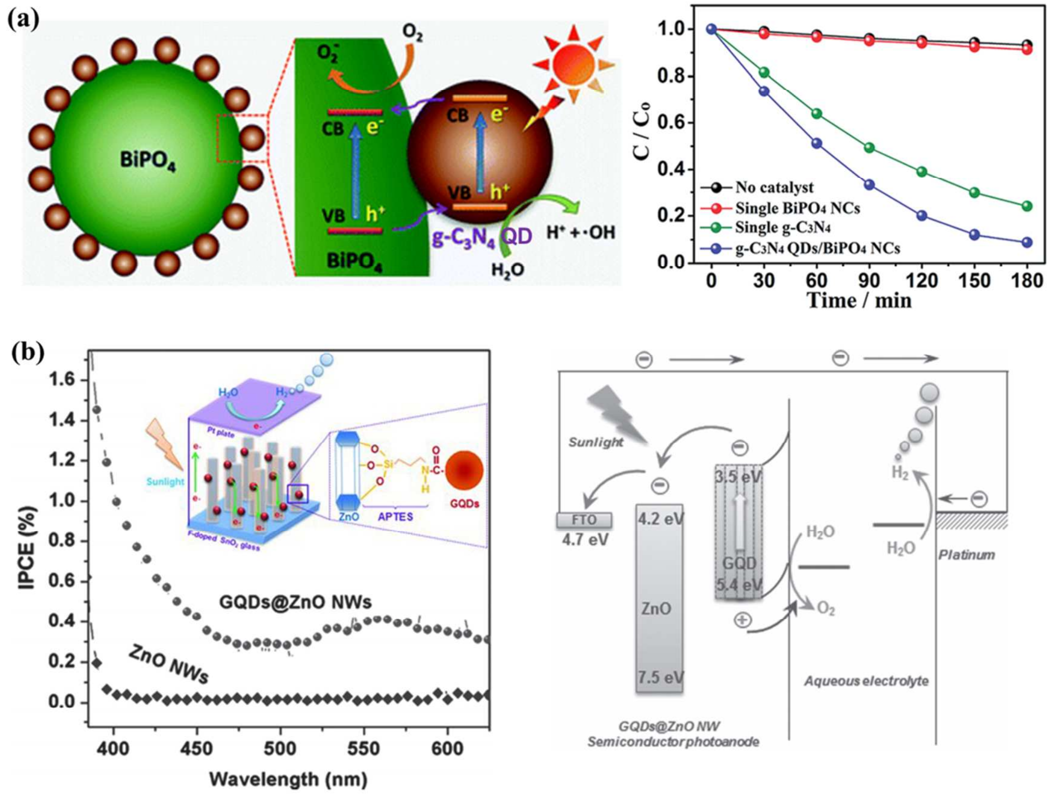

Fig. 9 (a) Schematic of charge separation at g-C_3N_4 QD/$BiPO_4$ interface and the photocatalytic activity of g-C_3N_4 QD/$BiPO_4$ hybrid for MO degradation. Adapted with permission from ref. 59. Copyright (2014) Royal Society of Chemistry. (b) Photo to current conversion efficiency spectra of GQDs@ZnO NWs photoelectrode-based device and its schematic of photoelectrochemical water splitting process. Adapted with permission from ref. 131. Copyright (2013) Wiley Publishing Group.

Liu *et al.* prepared MoS_2 QD (diameter of ~10 nm and thickness of ~5 nm) modified TiO_2 nanobelts (TiO_2-MoS_2) by a two-step hydrothermal method.[127] Evaluated by photodegradation of Rhodamine B (RhB) under visible light irradiation, the TiO_2-MoS_2 is ~4 times more active than bare TiO_2. The introduction of MoS_2 QDs is believed to increase the charge separation, visible-light absorption, specific surface area, and photochemical active reaction sites. Making use of the reducing effect of photogenerated electrons from TiO_2 particles, Ho *et al.* prepared MoS_2 (or WS_2) QDs/TiO_2 hybrids by in-situ photoreduction deposition followed by thermal annealing.[128] The MoS_2 (or WS_2) QD photosensitizers can extend the absorption edge of TiO_2 from UV region (< 420 nm) to 700 (or 620) nm. Conversely to the absence of photocatalytic activity of pure TiO_2

or composite of TiO_2 and MoS_2 (or WS_2) powder under visible light, MoS_2 (or WS_2) QDs/TiO_2 hybrid demonstrates high catalytic activity for the photodegradation of MB (~40% in 4h) and 4-Chlorophenol (~ 50% in 4h). Gao *et al.* synthesized MoS_2 QD-graphene-TiO_2 composite, which can effectively photo-catalyze rhodamine B (80% in 80 min, much better than Ag-graphene-TiO_2 composite) with excellent photochemical stability.[65]

Although phosphorene can adsorb visible light because of small bandgap, it is highly sensitive to humidity and oxygen and thus not suitable to act as photocatalyst independently. Lee *et al.* have demonstrated that BP@TiO_2 hybrid photocatalysts have excellent photocatalytic activity and stability.[129] It has also been shown that h-BN can greatly enhance the photo-degradation activity of TiO_2 for RhB and MB because the negatively charged h-BN promotes the immigration of photogenerated holes to the surface of TiO_2.[130] Presumably, phosphorene QDs and h-BN QDs shall interact more intimately with TiO_2 nanoparticles and create better synergy in photocatalysis.

Guo *et al.* used GQD as the visible light absorber to sensitize ZnO nanowire array for photoelectrochemical water splitting (Fig. 9b inset).[131] GQD coating leads to a larger open circuit voltage (V_{oc}, 0.15 V *vs.* 0.08 V), short circuit current density (J_{sc}, 0.064 mA cm^{-2} *vs.* 0.008 mA cm^{-2}) and photo-to-current efficiency (PCE) (ca. 0.42% *vs.* 0.05%) (Fig. 9b).The improvement is because of GQD-enhanced visible light absorption, electron-hole pair generation, charge separation, and charge transport. Hong group reported the enhanced photoelectrochemical HER activity of Si electrode after being decorated by N-doped GQDs.[132] Under the simulated sunlight (AM 1.5 G, 100 mW cm^{-2}), N-doped GQD coating positively shifts the onset potential of the planar Si electrode by ca. 0.29 V. Later, the same group further improved the HER performance (PCE of 2.29%) by coating N-doped GQD on Si nanowire photoelectrode.[125] Doping by multiple heteroatom species can introduce both p- and n-type domains on a single GQD, which may form photochemical diodes whereby conferring GQD the ability to act as photocatalyst independently. For example, Teng and co-workers prepared N,O co-doped GQDs for visible light-driven water splitting.[85] The co-existence of N-induced n-type domain and O-induced p-type domain facilitates the electron-hole separation during the photocatalytic reaction. The same group further improved the HER performance (an apparent quantum yield of 12.8% under 420 nm light) by depositing Pt on N,O co-doped GQD as co-catalyst and suppressor to electron transfer from GQD to solution.[133] Wang *et al.* employed g-C_3N_4 QDs with upconversion PL behavior as the energy donor to enhance the visible-light-driven (λ>600 nm) photocatalytic activity of bulk g-C_3N_4 toward HER.[42] They also showed that g-C_3N_4 QD decoration on TiO_2 can bring a 51.8 times enhancement on H_2 production under visible light irradiation.

Due to the large bandgap (~5.5 eV), h-BN itself is not suitable for photocatalysis. But aromatic C doping can significantly reduce the bandgap of h-BN to 2.72 eV and make the resultant h-BCN capable for efficient photocatalytic water splitting and CO_2 reduction.[98] Moreover, B-hydrogenated h-BN has been theoretically predicted to have a bandgap of 2.24 eV and hence a potential metal-free photocatalyst for water splitting under visible-light.[134] Sa *et al.* theoretically found that the desirable bandgap (1.52 eV) and band edge alignment make phosphorene a potential photocatalyst for water splitting.[135] h-BN QDs and phosphorene QDs may be more attractive due to better water solubility and higher catalytic activities.

5 Energy storage and conversion

5.1 Supercapacitors

2D materials have been widely used for supercapacitors.[2, 106, 136, 137] Their QD derivatives are expected to be even better in many cases because of larger specific surface area, more electrochemically active sites, ease to be integrated with other nanomaterials, and being more amenable to solution-based processes. By electrophoretic deposition of GQDs on the interdigital Au finger microelectrodes, Liu *et al.* assembled a GQD-based symmetric micro-supercapacitor and obtained a high rate performance, fast power response, and good cycling stability (97.8% retention after 5000 cycles) (Fig. 10a).[138] At the current density of 15 $\mu A\ cm^{-2}$, a specific capacity of 534.7 $\mu F\ cm^{-2}$ with an energy density of 0.074 $\mu Wh\ cm^{-2}$ and power density of 7.5 $\mu W\ cm^{-2}$ was obtained. Changing aqueous electrolyte to ionic liquid electrolyte gave a further seven times higher power and energy density.

In order to increase the potential window, asymmetric micro-supercapacitors have been fabricated with one electrode coated with GQDs and another functionalized with highly pseudocapacitive nanomaterials (e.g., MnO_2, PANI).[138, 139] Hu *et al.* made a GQD/CNT composite film which exhibits a capacitance of 44 $mF\ cm^{-2}$ (double the capacitance of the bare CNT film) (Fig. 10b).[140] Chen *et al.* developed 3D graphene/GQD composite as an additive-free monolithic electrode for supercapacitor.[141] Surprisingly, introduction of GQDs brought a 10 times increment in the conductivity of the 3D graphene structure. A specific capacity of 268 F g^{-1} was achieved, representing >90% improvement over bare 3D graphene. By chemical oxidation of aniline in the presence of GQDs, Mondal *et al.* synthesized GQD-modified polyaniline nanotubes with high aspect ratio and surface-to-volume ratio, and obtained a high specific capacity of 1044 F g^{-1} at the current density of 1 A g^{-1}.[142] It has been shown that the specific surface area of GQDs can be further increased (by a factor of six) *via* KOH activation.[143] Rich zigzag edges and ultra-fine pores (< 1 nm) are formed on activated GQDs, leading to a 200% increase in capacitance (236 F g^{-1}) which is much larger than that of activated graphene (172 F g^{-1}). The better capacitive behavior of GQDs as compared with graphene sheets is resulted from their much more abundant ion-interacting edge, defect, and chemical moiety sites.

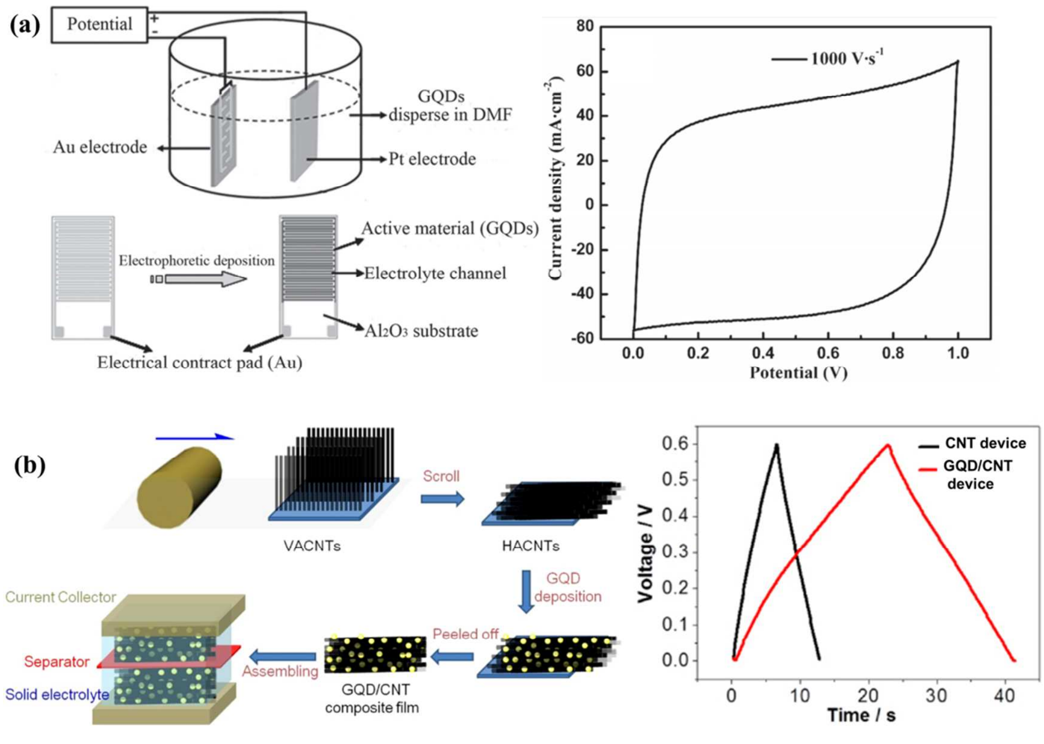

Fig. 10 (a) Fabrication of a symmetric microsupercapacitor by electrophoretic deposition of GQDs on interdigital finger electrode and its CV curve at 1000 V s^{-1}. Adapted with permission from ref. 138. Copyright (2013) Wiley Publishing Group. (b) Fabrication of a supercapacitor based on GQD/CNT composite film and its galvanostatic charge–discharge curve at 700 μA cm^{-2}. Adapted with permission from ref. 140. Copyright (2013) IOP Publishing Group.

g-C_3N_4 should have large capacity for charge storage because of rich graphitic N and pridinic N active sites, and abundant exchangeable protons attached to amine edges and oxygenated functional groups. Moreover, the intrinsically porous poly(tri-s-triazine) structure of g-C_3N_4 are advantageous for electrolyte transport and penetration. Therefore, bulk g-C_3N_4 materials and composites have been employed for supercapacitor development.[137, 144, 145] The aforementioned advantages of g-C_3N_4 should be more prominent for g-C_3N_4 QDs. However, g-C_3N_4 QDs can only work well by compositing with conducting materials (e.g., graphene) due to their poor conductivity.

In h-BN, the difference in electronegativity of B and N makes B-N bond partially ionic.[146] Therefore, B and N atoms have different oxidation states giving h-BN inherent pseudocapacitive property.[147] The pseudocapacitance of h-BN QDs should be higher resulting from the abundant B and N active edge sites. $B_xC_yN_z$ with adjustable B, C and N content and arrangement offers a wide range of electrochemical properties and good supercapacitive behavior.[148] $B_xC_yN_z$ QDs shall fill the gap between GQDs and h-BN QDs.

Edge-oriented MoS_2 films with sponge-like morphologies (*via* reaction of sulfur vapor with anodically formed Mo oxide sponge-like films) show good supercapacitive performance contributed by abundant active edges, cation intercalation into the inter- and intra-layer of MoS_2, redox reaction between different valence states of Mo.[149] Acerce *et al.* showed that chemically exfoliated 1T phase of MoS_2 nanosheets have favorable electrochemical properties for supercapacitor, such as intrinsic hydrophilicity, high electrical conductivity, permission for efficient cation intercalation (e.g. H^+, Li^+, Na^+ and K^+), and amenability for high-voltage (3.5 V) operation in non-aqueous organic electrolytes with excellent stability.[106] However, the potential of TMD QDs in supercapacitor applications are yet to be explored.

5.2 Batteries

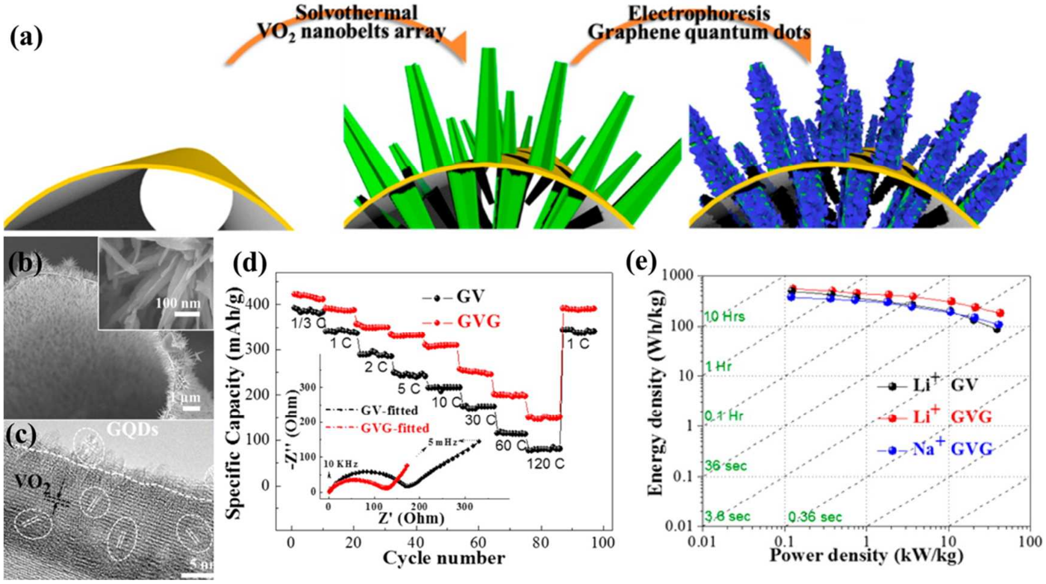

Fig. 11 (a) Fabrication of 3D graphene supported GQD-coated VO_2 nanobelts array (GVG). (b and c) SEM and HRTEM images of the hybrid structure. (d) Rate performance of the as-fabricated electrodes without (GV) or with (GVG) GQD coating. Inset is AC impedance plots. (e) Ragone plot of GVG electrode for Li and Na ion batteries (based on the total mass of the whole electrode). Adapted with permission from ref. 150. Copyright (2014) American Chemical Society.

Fan and co-workers have synthesized GQD-anchored VO_2-nanobelt array on 3D graphene as the cathode material of Li-ion battery (LIB) (Fig. 11 a-c).[150] This electrode gives a high specific capacity of 421 mAh g^{-1} at the current density of 1/3 C (1C=300 mA g^{-1}), ≥99% Coulomic efficiency, and good rate performance (reversible capacity of 151 mAh/g at 120 C), outperforming the 3D graphene/VO_2 electrode without GQDs (Fig. 11d). Moreover, the GQD-anchored electrode shows greatly enhanced stability (94% retention after 1500 cycles at 60 C), in contrast to the poor cyclability of other VO_2 based electrodes. Such electrode also well-performs as the cathode for sodium-ion battery (306 mAh g^{-1} at 1/3 C and 88% retention after 1500 cycles at 60 C). And at a high charge-discharge rate of 120 C, the electrode attains a power density of 42 kW kg^{-1} with a high energy density (>100 Wh kg^{-1}) (Fig. 11e). The same group has also similarly prepared CuO + Cu + GQD (CCG) triaxial nanowire arrays as the anode material for LIB, which offers a larger specific capacity (780 mAh g^{-1} at 1/3 C and 330 mAh g^{-1} at 30 C) than that of CuO + Cu (CC) electrode.[151] In both works, the GQD enhanced performance arises from several reasons. Firstly, GQD layer protects the active materials from forming solid electrolyte interface (SEI) film (especially in the first cycle), which ensures a high Coulombic efficiency. Secondly, conformal wrapping of GQDs on the surface of active nanomaterials improves the charge collection efficiency and conductivity of the electrode, which is crucial for high rate performance. Moreover, GQDs confer the electrode a rough surface, leading to a large surface area for metal ion storage. Finally, GQDs act as stabilizer to suppress the agglomeration and dissolution of electrode active materials, which is important for long cycling life of the electrode.

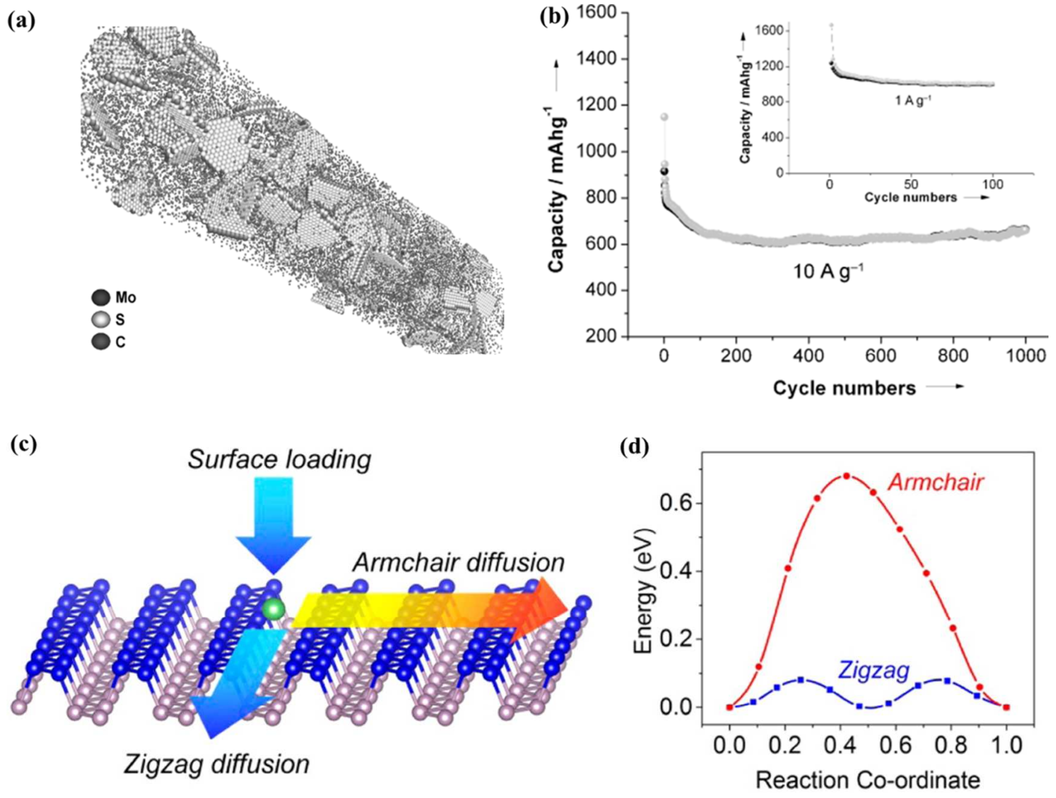

Fig. 12 (a) Schematic representation of single-layered MoS_2 QDs embedded carbon nanofiber. (b) Cycling performance of MoS_2 QDs-carbon nanofiber composite for lithium batteries. (a and b) adapted with permission from ref. 154. Copyright (2014) Wiley Publishing Group. (c) Schematic of Li adsorption and diffusion on the surface of phosphorene. (d) Energy profiles of Li diffusion along armchair and zigzag directions of phosphorene. (c and d) adapted with permission from ref. 157. Copyright (2015) American Chemical Society.

MoS_2 and its composites have been proved to be a highly desirable material for LIBs. For example, a high reversible capacity of 1290 mAh g^{-1} has been reported for MoS_2/graphene anode.[152] But the performance of MoS_2 batteries is generally compromised by substantial volume expansion, pulverization and aggregation of MoS_2 materials.[153] This is even more severe for sodium ion batteries because Na^+ is larger than Li^+. MoS_2 QDs should be less susceptible to these problems. In addition, due to the small sizes of QDs, the interfacial storage, insertion and conversion processes of Li^+ or Na^+ ions become highly reversible. Furthermore, MoS_2 QDs can be more easily and uniformly dispersed in the conducting matrix. Zhu *et al.* synthesized single-layered MoS_2 QD (diameter ~4 nm) embedded carbon nanofibers (diameter ~50 nm) using electrospinning and thermal annealing (Fig. 12a).[154] LIB anode based on such material shows the remarkable rate performance and discharge capacity (1007 mAh g^{-1} after 100 cycles at 1A g^{-1}; 661 mAh g^{-1} even after 1000 cycles at 10 A g^{-1}) (Fig. 12b). This electrode is also outstanding for sodium ion storage. Li atoms or ions can well disperse on g-C_3N_4 and can readily pass through the intrinsic pores of g-C_3N_4 with low energy barrier.[144, 155] Liu *et al.* demonstrated that oxygenated g-C_3N_4 (O 21.52 wt% and N 14.47 wt%) can be used as sulfur host for Li-S battery because the intrinsic porous nature of oxygenated g-C_3N_4, graphitic N, ether O, and carboxylic O on carbon nitride sheet favor trapping and reaction of polysulfide.[156]

Phosphorene is believed to be a promising anode material in batteries. DFT calculations show that Li atoms stably interact with phosphorus atoms in phosphorene.[157, 158] Due to the low energy barrier, Li atoms are able to diffuse in an ultrafast speed along the zigzag direction of phosphorene (Fig. 12c and d), which is estimated to be 10^2 or 10^4 times faster than that on MoS_2 or graphene sheet, respectively.[157-159] Interestingly and desirably, Li intercalation changes phosphorene from semiconducting to metallic. Furthermore, phosphorene is able to operate at high voltages (up to ~2.9 V). Phosphorene is also theoretically predicted to be promising for Na-ion battery, with the high theoretical capacity of 865 mAh g^{-1} with sodiation form of NaP or 433 mAh g^{-1} with sodiation form of NaP_2.[159] Sandwiched phosphorene – graphene hybrid has been prepared as the cathode for Na-ion battery, which gives a high specific capacity of 2,440 mA h g^{-1} (calculated using the mass of phosphorene only) at a current density of 0.05 A g^{-1} with good cycling stability (83% capacity retention after 100 cycles).[160] In view of the interesting progress for these 2D sheets (MoS_2, g-C_3N_4, and phosphorene), the possible applications of their QD forms for batteries are appealing. As compared to 2D sheets, the 2D-QDs should be more electrochemically active and the mechanical stress induced by ion intercalation and binding should be much reduced, therefore possibly leading to improved capacity and cycling stability for Li-ion or Na-ion batteries.

5.3 Photovoltaics

Taking the advantages of certain electronic or optical (adsorption and emission) properties, 2D-QDs may serve in the different components for photovaltaics, including active layer, hole transport layer, sensitizer, catalyst or co-catalyst for counter electrode. For example, Gao *et al.* fabricated a Si/GQD heterojunction solar cell using GQDs as the active layer, which promotes electron-hole separation and suppresses charge recombination (Fig. 13a).[161] The device shows a photo conversion efficiency (PCE) of 6.63%, much higher than that of bare Si device (2.26%) or the device using GO sheets as the active layer (3.99%). In a GQD/ZnO nanowire bulk heterojunction (BHJ) solid-state solar cell, the electron injection from GQDs to ZnO nanowires can boost the short-circuit current density (Jsc) by 75 times as compared with the bare ZnO nanowire based device.[162] However, limited GQD contacts with the hole transporting layer in this solar cell cause a low hole collection efficiency and consequently a low PCE. Tavakoli *et al.* prepared quasi core/shell PbS QD/GQD hybrids *via* a hot injection approach (Fig. 13b).[163] In comparison with the commonly used capping molecules (e.g. oleic acid and 3-mercaptopropionic acid) that hinder charge carrier transport in PbS QD films, the incomplete surface passivation of PbS QDs by an ultrathin layer of GQDs decreases the amount of trap states and promotes faster charge carrier extraction. The BHJ solar cells with PbS QD/GQD as the active layer deliver a higher current density (13.4 mA cm^{-2}), open voltage (0.58 V) and PCE (3.6%) than the devices based on the organic molecule capped PbS QDs (Fig. 13b).[163] The PCE of PbS QD/GQD device can be further improved to 4.1% by doping PbS QD with Cd.

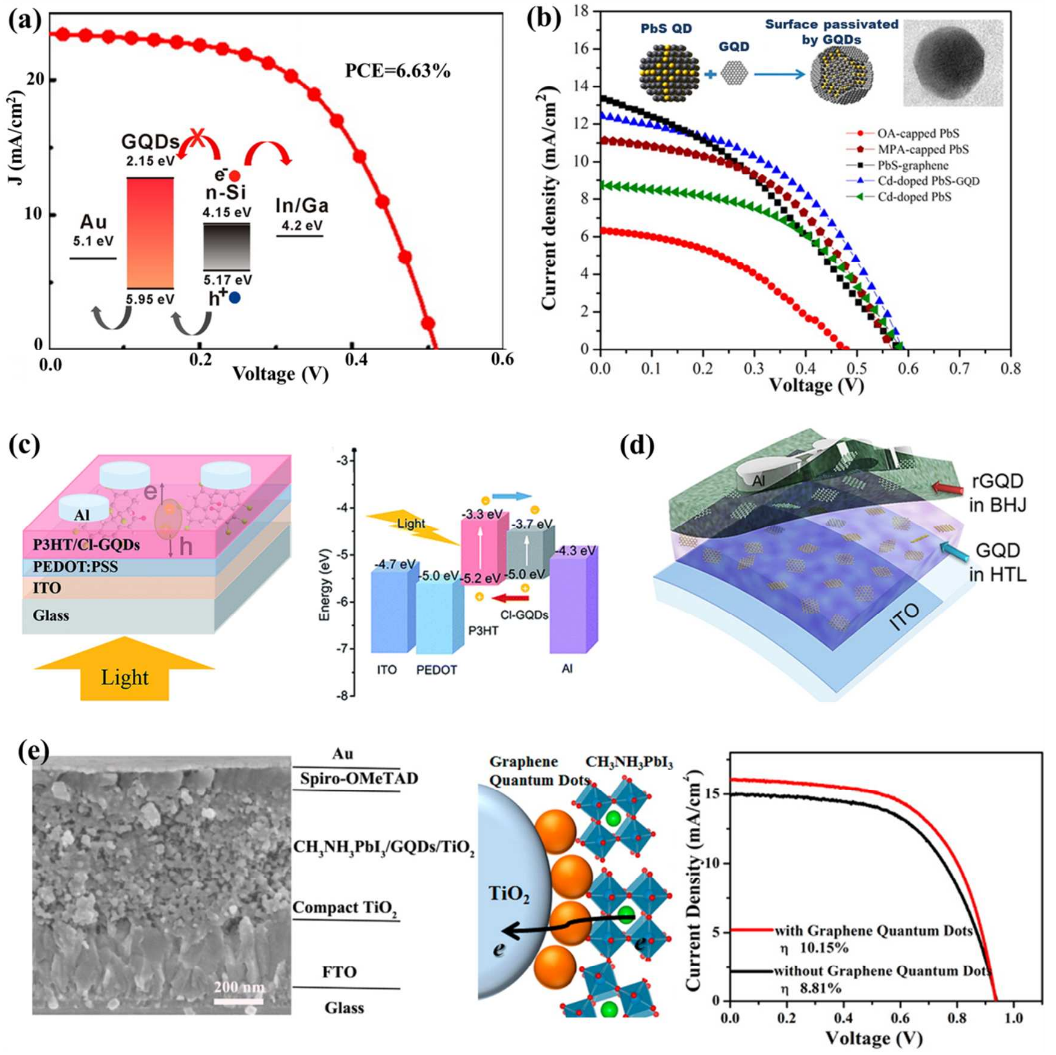

Fig. 13 (a) The J-V curve of CH_3−Si/GQDs heterojunction solar cell under AM1.5G. Inset shows its band diagram. Adapted with permission from ref. 161. Copyright (2014) American Chemical Society. (b) Schematic model of GQD-wrapped PbS QD and the J-V curves of PbS-based solar cells under AM1.5G. Adapted with permission from ref. 163. Copyright (2014) American Chemical Society. (c) Illustration of the Cl-GQD based photovoltaic device and its working mechanism. Adapted with permission from ref. 165. Copyright (2015) Royal Society of Chemistry. (d) Schematic illustration of organic photovoltaic device with hydrothermally reduced GQDs in BHJ layer and GQDs in HTL. Adapted with permission from ref. 168. Copyright (2015) Nature Publishing Group. (e) Cross-sectional SEM image of perovskite solar cell (left), schematic of its working mechanism (middle) and the J-V curves of the device with or without GQDs (right). Adapted with permission from ref. 175. Copyright (2014) American Chemical Society.

Using GQDs as the electron acceptor, Qu and coworkers developed BHJ polymer solar cells with a structure of ITO/PEDOT:PSS/P3HT:GQD/Al.[164] In the P3HT:GQD active layer, numerous p–n junctions are formed, which facilitate the dissociation of photogenerated excitons and electron transfer. Theoretically, the introduction of GQDs can improve the open circuit voltage (V_{oc}) from 0.5 V to 0.8 V. The actual device can achieve a PCE of 1.28% with V_{oc} of 0.67 V and J_{sc} of 6.33 mA cm^{-2}. Zhao *et al.* prepared Cl-doped GQDs by a liquid exfoliation method and showed that the addition of these QDs to P3HT active layer increases the charge carrier concentration of the polymer solar device by 30% and decreases the depletion layer width of the device (the working mechanism of the device is shown in Fig. 13c).[165] Gupta *et al.* used aniline functionalized GQDs (ANI-GQDs) as the uniformly-dispersed filler of organic polymers (P3HT) for a photovoltaic device.[166] The device with the structure of ITO/PEDOT:PSS/P3HT:ANI-GQDs/LiF/Al gives a PCE of 1.14%, superior to that of the control device with P3HT:ANI-graphene sheet as the active layer (PCE of 0.65%). Because of the larger size of graphene sheets than GQDs (a few μm *vs.* a few nm), P3HT:ANI-graphene mixture film is much rougher than P3HT:ANI-GQD film suggesting the large-scale phase separation exceeding the diffusion length of excitons, hence, its inferior performance. By adding GQDs with different abundance of oxygenated groups to the PTB7: $PC_{71}BM$ active layer of a BHJ solar cell, Kim *et al.* found that the improvement of optical absorptivity by rich oxygen functional groups of GQDs can lead to a considerably enhanced J_{sc}, while the efficient charge carrier extraction benefited from the better conductivity of less-oxidized GQDs can enhance fill factors (FF).[167] By balancing these two aspects, a maximum PCE of 7.6% has been achieved. The same group also found that the incorporation of GQDs in PEDOT:PSS hole transporting layer (HTL) improved the J_{sc} of the BHJ device from 15.6 mA cm^{-2} to 17.3 mA cm^{-2}, which can be attributed to the improved carrier conductance in the ITO/PEDOT:PSS due to the interaction between positively charged PEDOT and negatively GQDs.[168] To realize the synergistic effects, GQDs and hydrothermally reduced GQDs were added respectively to the PEDOT:PSS HTL and PTB7: $PC_{71}BM$ active layer (Fig. 13d) and an largely enhanced PCE (8.67%) was achieved.

Li *et al.* reported that GQD film with homogenous morphology, good conductivity and well-matched work function (4.9 eV) with the HOMO level of P3HT (5.0 eV) can be used independently as the efficient HTL for organic solar cell.[169] Compared with the device with graphene oxide (GO) sheets as the hole transport layer, GQD-based device offers an enhanced FF (66.3% *vs.* 55.4%) and PCE (3.51% *vs.* 2.27%). Although the conventional solar cells based on PEDOT:PSS have similar performance, their performance often quickly degrades because of the high acidity and hygroscopic properties of PEDOT:PSS. The same authors have also demonstrated the use of GQD film as the HTL in a small-molecule solar cell with DR3TBDT as the donor and $PC_{71}BM$ as the acceptor, which has achieved a high PCE of 6.82% along with good stability.[169] Similarly, Ding *et al.* reported that GQD HTL outperforms PEDOT:PSS and GO layer in the polymer solar cell device with PTB7:$PC_{71}BM$ or PCDTBT:$PC_{71}BM$ as active layer.[170] The improved performance can be attributed to better transmittance of GQD layer than PEDOT:PSS layer and better Ohmic contact between GQDs and donor polymers because of the higher work function of GQD than GO.

Yan *et al.* have used chemical-group-free GQDs made using a bottom-up organic synthesis approach to sensitize the TiO_2 photoanode in solar cell.[50] However, the low binding affinity of GQDs with TiO_2 causes a J_{sc} two-order of magnitude lower than the dye-sensitized solar cell (DSSC) based on ruthenium complex photosensitive dye. But we speculate that the performance will be greatly improved if GQDs with oxygen groups, which can interact well with TiO_2, are used.[74, 75] Fang *et al.* used GQDs as the co-sensitizer together with conventional N719 dye for TiO_2 photoanode and observed the increase of PCE from 4.9 to 6.10% and increase of J_{sc} from 9.72 to 14.07 mA cm^{-2}.[171] Similarly, Mihalache *et al.* increased J_{sc} and PCE of DSSC device using N-doped GQDs as the co-sensitizer with N3 Ru-dye.[172] The enhanced performance can be attributed to the enhanced charge separation, suppressed electron recombination to the redox couple in electrolyte, and overlapped PL spectrum of GQDs with the absorption spectrum of N3 Ru-dye. Lee *et al.* deposited GQDs with upconversion PL onto TiO_2 to increase the amount of light being utilized by DSSC, making the PCE of the device increases from 7.28 to 9.2%.[173]

Instead of taking the advantages of GQD's optical properties, Chen *et al.* improved the PCE of a DSSC by making the polypyrrole counter electrode highly porous after introduction of GQDs (comparable to that of Pt counter electrode-based device).[174] In a recently reported perovskite solar cell with the structure of $CH_3NH_3PbI_3$/GQDs/TiO_2, the introduction of an ultrathin layer of GQDs improves the PCE from 8.81to 10.15% and J_{sc} from 17.07 to 15.34 mA cm^{-2} (Fig. 13e).[175] The improved performance is due to a nearly 3 times faster electron extraction (90-106 ps), which ensures an enhanced photon-to-current conversion in the visible-NIR regions and 75% PL quenching of perovskite-TiO_2 film.

Phosphorene shows promise for optoelectronic applications due to its high hole mobility (up to 1000 cm^2 V^{-1} S^{-1}), narrow direct bandgap (0.3 - 1.5 eV depending on the number of layers), and bipolar characteristics.[176] Deng *et al.* fabricated an electrically-tunable p-n diode for photovoltaic energy conversion based on the heterojunction between p-type few-layer phosphorene and n-type monolayer MoS_2, with a PCE of 0.3%.[177] Reducing the thickness of few-layer phosphorene to double-layer has been theoretically predicted to increase the PCE of a p-n diode to 18%.[176] On the basis of bipolar feature of few-layer phosphorene, Buscema *et al.* fabricated a p-n heterojunction on a single phophorene sheet with two regions differently biased through two h-BN dielectric gates.[110] The photovoltaic effect is extended to NIR region (up to 940 nm). In terms of electrical properties, phosphorene fills the gap between graphene and TMDs. Therefore, phosphorene QDs shall fill the application gap between GQDs and TMD-QDs.

6 Summary and perspectives

Quantum dots derived from the atomically-thin two-dimensional sheets are emerging zero-dimensional materials. Complementing with each other, these 2D-QDs cover a wide range of interesting physicochemical properties (optical, catalytic, chemical, electrochemical, electronic, etc.). While inheriting some unique structural and physicochemical properties of their 2D counterparts, 2D-QDs often gain additional advantages for certain applications due to their lower dimension. Firstly, their properties are more sensitively tunable by size, thickness, edge configurations, defects, chemical functionalities, covalently incorporated heteroatom dopants, or adsorbed molecular dopants. This could lead to the rise of new properties. Their properties are also more sensitive to local minute perturbations or interactions. This is desirable for sensor development. In addition, these QDs have better solubility, thus better amenability for solution-based processes. Moreover, it is often easier to hybridize them with other functional nanomaterials. Finally, small size is a key advantage if these QDs are to be used as the fluorescent tags on molecular targets for imaging purposes because the dynamics and functions of the targets may be altered by large tags.

Equipped with a wide range of extraordinary properties, 2D-QDs hence promise a broad spectrum of novel applications. Although this article places the emphasis on catalysis and energy applications, 2D-QDs are also promising for bioimaging, optical sensing, drug delivery, photodynamic therapy, electrochemical sensors, display, optoelectronics, etc. The biological applications of GQDs have been comprehensively reviewed in our recent article.[7] Particularly to be mentioned, with unique combination of several key merits (including high photostability, highly tunable PL, molecular size, biocompatibility, ease to be conjugated with biomolecules), GQDs are superior to the conventional organic fluorophores and widely used semiconductor QDs for various bio-imaging purposes.[7, 178, 179] For example, Zheng *et al.* have used insulin-functionalized GQD to visualize the distribution and dynamics of insulin receptors in live adipocytes.[180] Although GQDs for bio-imaging have been demonstrated by many laboratories, the potentials of other 2D-QDs have not yet been extensively explored. Non-specific cellular imaging in a number of cell types has been demonstrated using MoS_2 QDs, WS_2 QDs, or h-BN QDs, suggesting their potentials in bio-imaging.[14, 27-29, 35] Zhang *et al.* demonstrated that single-layered g-C_3N_4 QDs can emit stable and strong two-photon fluorescence, and can effectively penetrate into and be trapped in the nuclei of HepG2 cells due to the interaction with chromatin whereby allowing selective two-photon imaging of cellular nucleus.[45]

Recently, Wang and co-workers showed that $MoSe_2$ QDs can be used for photothermal therapy due to their small size, strong NIR adsorption, high photothermal conversion efficiency, good biocompatibility, colloidal stability and photostability.[33] Yong *et al.* found that WS_2 QDs can serve simultaneously as the photothermal agent as well as the radiosensitizer for synergistic radiation and photothermal therapy both *in vitro* and *vivo*.[38] Moreover, the strong NIR absorption and X-ray attenuation make WS_2 QDs desirable contrast imaging agent to visualise biological tissues *via* photoacoustic imaging and X-ray computed tomography. Sun *et al.* reported the outstanding photothermal performance of phosphorene QDs.[49]

GQDs have been employed for various sensitive optical sensors.[22, 181, 182] Several studies have also demonstrated the potential of other 2D-QDs. For example, g-C_3N_4 QDs and its O,S co-doped derivatives have been used as effective fluorescent probes for label-free detection of Cu^{2+}, Fe^{3+} or Hg^{2+} based on PL quenching upon the strong binding of these metal ions with N, O and/or S functional groups of g-C_3N_4 QDs.[44, 60] Zhou *et al.* attributed the PL quenching of g-C_3N_4 QDs by Fe^{3+} to the unique redox potential of Fe^{3+} lying between the valence and conduction band of g-C_3N_4 QDs which facilitates the photo-induced electron transfer from g-C_3N_4 QDs.[46] Tang *et al.* designed an interesting chemiluminescence (CL) sensor for selective detection of free chlorine in water which induces strong emission from g-C_3N_4 QDs.[58] Using MoS_2 QDs as the PL probes, Wang *et al.* demonstrated sensitive and selective detection of 2,4,6-trinitrophenol (TNP).[62]

GQDs have demonstrated good potential for electronics and optoelectronics.[19, 183] Song *et al.* fabricated GQD-based light-emitting diodes (LEDs).[184] Zhang *et al.* have shown that TMD QDs (e.g. $MoSe_2$, WS_2 and $NbSe_2$ QDs) and phosphorene QDs can be mixed with polyvinylpyrrolidone as the active layer for memory devices, which exhibited a nonvolatile write-once-read-many behavior with high ON/OFF ratio and good stability.[30, 47] Zhou and coworkers demonstrated that g-C_3N_4 QDs can be utilized as photoconductor in an all-solid-state device.[46]

The family of 2D materials is still growing. Similar to phosphorene, silicene, germanene and stanene have also attracted research interest.[185] The poor stability of these bulked 2D materials still remains as the greatest challenge for practical applications.[186] But it can be improved after being hydrogenated. Recently, Gogotsi and coworkers have synthesized a class of 2D materials, specifically, early transition metal carbides and carbonitride (MXenes, where M is early transition metal and X is C or N), such as, Ti_3C_2, Ti_2C, Nb_2C, V_2C, $(Ti_{0.5}Nb_{0.5})_2C$, $(V_{0.5},Cr_{0.5})_3C_2$, Ti_3CN, and Ta_4C_3.[187] The electronic properties of these MXenes can be tuned by changing their elemental composition and/or surface terminations. Very recently, Yang group reported the solution-phase growth of atomically thin two-dimensional organic-inorganic hybrid perovskites. The continuous growth of 2D family naturally increases the variety of 2D-QDs.[188]

Despite the great progress has been made, the research of 2D-QDs is still at the early stage and many challenges are waiting to be tackled. Considering that the properties of 2D-QDs are highly sensitive to size, edge configurations, chemical functionalities and heteroatom dopants, developing synthetic methods to precisely control these parameters are much needed. However, this ambition has to be balanced by the needs for large-scale and low-cost production in often cases. The understanding on the catalytic, electrochemical, optical, and electrical properties of 2D-QDs is still much limited and sometimes even controversial because of the large heterogeneity of currently synthesized QDs and because of the lack of experimental studies to characterize them at single particle level. The practical use of 2D-QDs requires careful consideration on their chemical and electrochemical stability. But the studies on this regard are limited. Phosphorene QDs are easily oxidized in air and water. TMD-QDs (particularly $MoTe_2$ QD) can also be oxidized in air to various extents.[189] In addition, when TMD-QDs are used as electrocatalysts, it should be noted that they are fully stable only within a small potential window.[190] When 2D-QDs are used as the fluorescent reporters, their relatively low quantum yield and broad emission band could be problematic as compared with the conventional fluoropores. The former may be tackled by reducing the surface traps, and introducing passivation layer, dopants, or chemical functionalities. The latter issue can be eliminated by synthesize QDs with narrow property distribution. We hope this article will stimulate the development of this emerging and exciting field.

Acknowledgement

We thank the support from Ministry of Education of Singapore under an AcRF Tier 2 grant (MOE2014-T2-2-003, ARC31/14).

References

1. Y. X. Liu, X. C. Dong and P. Chen, *Chem. Soc. Rev.*, 2012, **41**, 2283-2307.
2. X. W. Wang, G. Z. Sun, P. Routh, D. H. Kim, W. Huang and P. Chen, *Chem. Soc. Rev.*, 2014, **43**, 7067-7098.
3. F. Bonaccorso, L. Colombo, G. H. Yu, M. Stoller, V. Tozzini, A. C. Ferrari, R. S. Ruoff and V. Pellegrini, *Science*, 2015, **347,** 1246501.
4. S. Z. Butler, S. M. Hollen, L. Y. Cao, Y. Cui, J. A. Gupta, H. R. Gutierrez, T. F. Heinz, S. S. Hong, J. X. Huang, A. F. Ismach, E. Johnston-Halperin, M. Kuno, V. V. Plashnitsa, R. D. Robinson, R. S. Ruoff, S. Salahuddin, J. Shan, L. Shi, M. G. Spencer, M. Terrones, W. Windl and J. E. Goldberger, *Acs Nano*, 2013, **7**, 2898-2926.
5. H. Zhang, *Acs Nano*, 2015, **9**, 9451-9469.
6. M. S. Xu, T. Liang, M. M. Shi and H. Z. Chen, *Chem. Rev.*, 2013, **113**, 3766-3798.
7. X. T. Zheng, A. Ananthanarayanan, K. Q. Luo and P. Chen, *Small*, 2015, **11**, 1620-1636.
8. Z. F. Wang, H. D. Zeng and L. Y. Sun, *J. Mater. Chem. C*, 2015, **3**, 1157-1165.
9. H. J. Sun, L. Wu, W. L. Wei and X. G. Qu, *Mater. Today*, 2013, **16**, 433-442.
10. Z. P. Zhang, J. Zhang, N. Chen and L. T. Qu, *Energ Environ. Sci.*, 2012, **5**, 8869-8890.
11. J. H. Shen, Y. H. Zhu, X. L. Yang and C. Z. Li, *Chem. Commun.*, 2012, **48**, 3686-3699.
12. T. F. Jaramillo, K. P. Jorgensen, J. Bonde, J. H. Nielsen, S. Horch and I. Chorkendorff, *Science*, 2007, **317**, 100-102.
13. T. Y. Wang, D. L. Gao, J. Q. Zhuo, Z. W. Zhu, P. Papakonstantinou, Y. Li and M. X. Li, *Chem.-Eur. J.*, 2013, **19**, 11939-11948.
14. S. J. Xu, D. Li and P. Y. Wu, *Adv. Funct. Mater.*, 2015, **25**, 1127-1136.

15. X. P. Wang, L. X. Wang, F. Zhao, C. G. Hu, Y. Zhao, Z. P. Zhang, S. L. Chen, G. Q. Shi and L. T. Qu, *Nanoscale*, 2015, **7**, 3035-3042.
16. L. H. Zhang and Z. H. Guo, *Acta Chim. Sinica*, 2013, **71**, 644-648.
17. X. Yan, B. S. Li and L. S. Li, *Accounts Chem. Res.*, 2013, **46**, 2254-2262.
18. L. L. Li, G. H. Wu, G. H. Yang, J. Peng, J. W. Zhao and J. J. Zhu, *Nanoscale*, 2013, **5**, 4015-4039.
19. M. Bacon, S. J. Bradley and T. Nann, *Part. Part. Syst. Char.*, 2014, **31**, 415-428.
20. S. J. Zhu, Y. B. Song, X. H. Zhao, J. R. Shao, J. H. Zhang and B. Yang, *Nano Res.*, 2015, **8**, 355-381.
21. Y. Q. Dong, C. Q. Chen, X. T. Zheng, L. L. Gao, Z. M. Cui, H. B. Yang, C. X. Guo, Y. W. Chi and C. M. Li, *J. Mater. Chem.*, 2012, **22**, 8764-8766.
22. A. Ananthanarayanan, X. W. Wang, P. Routh, B. Sana, S. Lim, D. H. Kim, K. H. Lim, J. Li and P. Chen, *Adv. Funct. Mater.*, 2014, **24**, 3021-3026.
23. H. Park, S. H. Noh, J. H. Lee, W. J. Lee, J. Y. Jaung, S. G. Lee and T. H. Han, *Sci. Rep.-Uk*, 2015, **5**, 14163.
24. L. X. Lin and S. W. Zhang, *Chem. Commun.*, 2012, **48**, 10177-10179.
25. S. J. Zhuo, M. W. Shao and S. T. Lee, *Acs Nano*, 2012, **6**, 1059-1064.
26. L. Wang, X. Chen, Y. L. Lu, C. X. Liu and W. S. Yang, *Carbon*, 2015, **94**, 472-478.
27. L. X. Lin, Y. X. Xu, S. W. Zhang, I. M. Ross, A. C. M. Ong and D. A. Allwood, *Small*, 2014, **10**, 60-65.
28. Z. Y. Lei, S. J. Xu, J. X. Wan and P. Y. Wu, *Nanoscale*, 2015, **7**, 18902-18907.
29. H. Li, R. Y. Tay, S. H. Tsang, X. Zhen and E. H. Teo, *Small*, 2015, **11**, 6491-6499.
30. X. Zhang, Z. C. Lai, Z. D. Liu, C. L. Tan, Y. Huang, B. Li, M. T. Zhao, L. H. Xie, W. Huang and H. Zhang, *Angew. Chem. Int. Ed.*, 2015, **54**, 5425-5428.
31. D. Gopalakrishnan, D. Damien and M. M. Shaijumon, *Acs Nano*, 2014, **8**, 5297-5303.
32. Z. X. Gan, L. Z. Liu, H. Y. Wu, Y. L. Hao, Y. Shan, X. L. Wu and P. K. Chu, *Appl. Phys. Lett.*, 2015, **106**.
33. L. H. Yuwen, J. J. Zhou, Y. Q. Zhang, Q. Zhang, J. Y. Shan, Z. M. Luo, L. X. Weng, Z. G. Teng and L. H. Wang, *Nanoscale*, 2015. DOI: 10.1039/C5NR08166A.
34. V. Stengl, J. Tolasz and D. Popelkova, *Rsc Adv.*, 2015, **5**, 89612-89620.
35. L. Lin, Y. Xu, S. Zhang, I. M. Ross, A. C. Ong and D. A. Allwood, *Acs Nano*, 2013, **7**, 8214-8223.
36. H. D. Ha, D. J. Han, J. S. Choi, M. Park and T. S. Seo, *Small*, 2014, **10**, 3858-3862.
37. W. Qiao, S. M. Yan, X. Y. Song, X. Zhang, Y. Sun, X. Chen, W. Zhong and Y. W. Du, *Rsc Adv.*, 2015, **5**, 97696-97701.
38. Y. Yong, X. J. Cheng, T. Bao, M. Zu, L. Yan, W. Y. Yin, C. C. Ge, D. L. Wang, Z. Gu and Y. Zhao, *Acs Nano*, 2015, **9**, 12451.
39. J. Y. Wu, X. Y. Zhang, X. D. Ma, Y. P. Qiu and T. Zhang, *Rsc Adv.*, 2015, **5**, 95178-95182.
40. B. L. Li, L. X. Chen, H. L. Zou, J. L. Lei, H. Q. Luo and N. B. Li, *Nanoscale*, 2014, **6**, 9831-9838.
41. D. Gopalakrishnan, D. Damien, B. Li, H. Gullappalli, V. K. Pillai, P. M. Ajayan and M. M. Shaijumon, *Chem. Commun.*, 2015, **51**, 6293-6296.
42. W. J. Wang, J. C. Yu, Z. R. Shen, D. K. L. Chan and T. Gu, *Chem. Commun.*, 2014, **50**,

10148-10150.

43. X. J. Bai, S. C. Yan, J. J. Wang, L. Wang, W. J. Jiang, S. L. Wu, C. P. Sun and Y. F. Zhu, *J. Mater. Chem. A*, 2014, **2**, 17521-17529.
44. S. W. Zhang, J. X. Li, M. Y. Zeng, J. Z. Xu, X. K. Wang and W. P. Hu, *Nanoscale*, 2014, **6**, 4157-4162.
45. X. D. Zhang, H. X. Wang, H. Wang, Q. Zhang, J. F. Xie, Y. P. Tian, J. Wang and Y. Xie, *Adv. Mater.*, 2014, **26**, 4438-4443.
46. Z. Zhou, Y. Shen, Y. Li, A. Liu, S. Liu and Y. Zhang, *Acs Nano*, 2015, **9**, 12480-12487.
47. X. Zhang, H. M. Xie, Z. D. Liu, C. L. Tan, Z. M. Luo, H. Li, J. D. Lin, L. Q. Sun, W. Chen, Z. C. Xu, L. H. Xie, W. Huang and H. Zhang, *Angew. Chem. Int. Ed.*, 2015, **54**, 3653-3657.
48. Z. Sofer, D. Bousa, J. Luxa, V. Mazanek and M. Pumera, *Chem. Commun. (Camb)*, 2015.
49. Z. B. Sun, H. H. Xie, S. Y. Tang, X. F. Yu, Z. N. Guo, J. D. Shao, H. Zhang, H. Huang, H. Y. Wang and P. K. Chu, *Angew. Chem. Int. Ed.*, 2015, **54**, 11526-11530.
50. X. Yan, X. Cui, B. S. Li and L. S. Li, *Nano Lett.*, 2010, **10**, 1869-1873.
51. Q. Q. Li, S. Zhang, L. M. Dai and L. S. Li, *J. Am. Chem. Soc.*, 2012, **134**, 18932-18935.
52. L. Wang, Y. L. Wang, T. Xu, H. B. Liao, C. J. Yao, Y. Liu, Z. Li, Z. W. Chen, D. Y. Pan, L. T. Sun and M. H. Wu, *Nat. Commun.*, 2014, **5**, 5357.
53. L. P. Lin, M. C. Rong, S. S. Lu, X. H. Song, Y. X. Zhong, J. W. Yan, Y. R. Wang and X. Chen, *Nanoscale*, 2015, **7**, 1872-1878.
54. J. Ju and W. Chen, *Biosens. Bioelectron.*, 2014, **58**, 219-225.
55. D. Qu, Z. C. Sun, M. Zheng, J. Li, Y. Q. Zhang, G. Q. Zhang, H. F. Zhao, X. Y. Liu and Z. G. Xie, *Adv. Opt. Mater.*, 2015, **3**, 360-367.
56. D. Qu, M. Zheng, L. G. Zhang, H. F. Zhao, Z. G. Xie, X. B. Jing, R. E. Haddad, H. Y. Fan and Z. C. Sun, *Sci. Rep.-Uk*, 2014, **4**, 5294.
57. X. M. Li, S. P. Lau, L. B. Tang, R. B. Ji and P. Z. Yang, *Nanoscale*, 2014, **6**, 5323-5328.
58. Y. R. Tang, Y. Y. Su, N. Yang, L. C. Zhang and Y. Lv, *Anal. Chem.*, 2014, **86**, 4528-4535.
59. Z. S. Li, B. L. Li, S. H. Peng, D. H. Li, S. Y. Yang and Y. P. Fang, *Rsc Adv.*, 2014, **4**, 35144-35148.
60. Y. C. Lu, J. Chen, A. J. Wang, N. Bao, J. J. Feng, W. P. Wang and L. X. Shao, *J. Mater. Chem. C*, 2015, **3**, 73-78.
61. H. Huang, C. C. Du, H. Y. Shi, X. Feng, J. Li, Y. L. Tan and W. B. Song, *Part. Part. Syst. Char.*, 2015, **32**, 72-79.
62. Y. Wang and Y. N. Ni, *Anal. Chem.*, 2014, **86**, 7463-7470.
63. X. P. Ren, L. Q. Pang, Y. X. Zhang, X. D. Ren, H. B. Fan and S. Z. Liu, *J. Mater. Chem. A*, 2015, **3**, 10693-10697.
64. H. H. Lin, C. X. Wang, J. P. Wu, Z. Z. Xu, Y. J. Huang and C. Zhang, *New J. Chem.*, 2015, **39**, 8492-8497.
65. W. Y. Gao, M. Q. Wang, C. X. Ran and L. Li, *Chem. Commun.*, 2015, **51**, 1709-1712.
66. H. O. Churchill and P. Jarillo-Herrero, *Nat. Nanotechnol.*, 2014, **9**, 330-331.

67. M. A. Sk, A. Ananthanarayanan, L. Huang, K. H. Lim and P. Chen, *J. Mater. Chem. C*, 2014, **2**, 6954-6960.

68. J. Sun, S. W. Yang, Z. Y. Wang, H. Shen, T. Xu, L. T. Sun, H. Li, W. W. Chen, X. Y. Jiang, G. Q. Ding, Z. H. Kang, X. M. Xie and M. H. Jiang, *Part. Part. Syst. Char.*, 2015, **32**, 434-440.

69. A. Ananthanarayanan, Y. Wang, P. Routh, M. A. Sk, A. Than, M. Lin, J. Zhang, J. Chen, H. D. Sun and P. Chen, *Nanoscale*, 2015, **7**, 8159-8165.

70. J. H. Shen, Y. H. Zhu, C. Chen, X. L. Yang and C. Z. Li, *Chem. Commun.*, 2011, **47**, 2580-2582.

71. Q. Feng, Q. Q. Cao, M. Li, F. C. Liu, N. J. Tang and Y. W. Du, *Appl. Phys. Lett.*, 2013, **102**, 013111.

72. M. Li, W. B. Wu, W. C. Ren, H. M. Cheng, N. J. Tang, W. Zhong and Y. W. Du, *Appl. Phys. Lett.*, 2012, **101**, 103107.

73. M. L. Mueller, X. Yan, B. Dragnea and L. S. Li, *Nano Lett.*, 2011, **11**, 56-60.

74. R. Long, *Chemphyschem*, 2013, **14**, 579-582.

75. K. J. Williams, C. A. Nelson, X. Yan, L. S. Li and X. Y. Zhu, *Acs Nano*, 2013, **7**, 1388-1394.

76. D. B. Shinde and V. K. Pillai, *Angew. Chem. Int. Ed.*, 2013, **52**, 2482-2485.

77. A. X. Zheng, Z. X. Cong, J. R. Wang, J. Li, H. H. Yang and G. N. Chen, *Biosens. Bioelectron.*, 2013, **49**, 519-524.

78. H. J. Sun, N. Gao, K. Dong, J. S. Ren and X. G. Qu, *Acs Nano*, 2014, **8**, 6202-6210.

79. H. J. Sun, A. D. Zhao, N. Gao, K. Li, J. S. Ren and X. G. Qu, *Angew. Chem. Int. Ed.*, 2015, **54**, 7176-7180.

80. X. M. Chen, G. H. Wu, J. M. Chen, X. Chen, Z. X. Xie and X. R. Wang, *J. Am. Chem. Soc.*, 2011, **133**, 3693-3695.

81. H. J. Yin, H. J. Tang, D. Wang, Y. Gao and Z. Y. Tang, *Acs Nano*, 2012, **6**, 8288-8297.

82. X. Yan, B. S. Li, X. Cui, Q. S. Wei, K. Tajima and L. S. Li, *J. Phys. Chem. Lett.*, 2011, **2**, 1119-1124.

83. J. Ju and W. Chen, *Anal. Chem.*, 2015, **87**, 1903-1910.

84. D. L. Jiang, Y. Zhang, H. Y. Chu, J. Liu, J. Wan and M. Chen, *Rsc Adv.*, 2014, **4**, 16163-16171.

85. T. F. Yeh, C. Y. Teng, S. J. Chen and H. S. Teng, *Adv. Mater.*, 2014, **26**, 3297-3303.

86. Y. Song and S. W. Chen, *Acs Appl. Mater. Inter.*, 2014, **6**, 14050-14060.

87. X. C. Wang, K. Maeda, A. Thomas, K. Takanabe, G. Xin, J. M. Carlsson, K. Domen and M. Antonietti, *Nat. Mater.*, 2009, **8**, 76-80.

88. X. T. Cao, J. Ma, Y. P. Lin, B. X. Yao, F. M. Li, W. Weng and X. C. Lin, *Spectrochim. Acta A*, 2015, **151**, 875-880.

89. J. Zhou, Y. Yang and C. Y. Zhang, *Chem. Commun.*, 2013, **49**, 8605-8607.

90. X. C. Wang, S. Blechert and M. Antonietti, *Acs Catal.*, 2012, **2**, 1596-1606.

91. J. J. Zhu, P. Xiao, H. L. Li and S. A. C. Carabineiro, *Acs Appl. Mater. Inter.*, 2014, **6**, 16449-16465.

92. Y. Zheng, J. Liu, J. Liang, M. Jaroniec and S. Z. Qiao, *Energ Environ. Sci.*, 2012, **5**, 6717-6731.

93. X. C. Wang, K. Maeda, X. F. Chen, K. Takanabe, K. Domen, Y. D. Hou, X. Z. Fu and

M. Antonietti, *J. Am. Chem. Soc.*, 2009, **131**, 1680-1681.

94. D. Krepel, L. Kalikhman-Razvozov and O. Hod, *J. Phys. Chem. C*, 2014, **118**, 21110-21118.
95. S. S. R. K. C. Yamijala, A. Bandyopadhyay and S. K. Pati, *J. Phys. Chem. C*, 2013, **117**, 23295-23304.
96. Y. Xi, M. W. Zhao, X. P. Wang, S. J. Li, X. J. He, Z. H. Wang and H. X. Bu, *J. Phys. Chem. C*, 2011, **115**, 17743-17749.
97. N. Kumar, K. Moses, K. Pramoda, S. N. Shirodkar, A. K. Mishra, U. V. Waghmare, A. Sundaresan and C. N. R. Rao, *J. Mater. Chem. A*, 2013, **1**, 5806-5821.
98. C. J. Huang, C. Chen, M. W. Zhang, L. H. Lin, X. X. Ye, S. Lin, M. Antonietti and X. C. Wang, *Nat. Commun.*, 2015, **6**, 7698.
99. Y. Xi, X. Y. Zhao, A. Z. Wang, X. P. Wang, H. X. Bu and M. W. Zhao, *Physica E*, 2013, **49**, 52-60.
100. A. Bandyopadhyay, S. S. R. K. C. Yamijala and S. K. Pati, *Phys. Chem. Chem. Phys.*, 2013, **15**, 13881-13887.
101. V. Stengl, J. Henych and M. Kormunda, *Sci. Adv. Mater.*, 2014, **6**, 1106-1116.
102. G. C. Loh, R. Pandey, Y. K. Yap and S. P. Karna, *J. Phys. Chem. C*, 2015, **119**, 1565-1574.
103. R. M. Clark, B. J. Carey, T. Daeneke, P. Atkin, M. Bhaskaran, K. Latham, I. S. Cole and K. Kalantar-zadeh, *Nanoscale*, 2015, **7**, 16763-16772.
104. P. Liang, T. Shen, H. B. Shu and S. Xing, *Solid State Commun.*, 2015, **218**, 25-30.
105. L. J. Cao, S. B. Yang, W. Gao, Z. Liu, Y. J. Gong, L. L. Ma, G. Shi, S. D. Lei, Y. H. Zhang, S. T. Zhang, R. Vajtai and P. M. Ajayan, *Small*, 2013, **9**, 2905-2910.
106. M. Acerce, D. Voiry and M. Chhowalla, *Nat. Nanotechnol.*, 2015, **10**, 313-318.
107. E. G. D. Firmiano, A. C. Rabelo, C. J. Dalmaschio, A. N. Pinheiro, E. C. Pereira, W. H. Schreiner and E. R. Leite, *Adv. Energy Mater.*, 2014, **4**, 1301380.
108. H. Liu, A. T. Neal, Z. Zhu, Z. Luo, X. F. Xu, D. Tomanek and P. D. D. Ye, *Acs Nano*, 2014, **8**, 4033-4041.
109. L. K. Li, Y. J. Yu, G. J. Ye, Q. Q. Ge, X. D. Ou, H. Wu, D. L. Feng, X. H. Chen and Y. B. Zhang, *Nat. Nanotechnol.*, 2014, **9**, 372-377.
110. M. Buscema, D. J. Groenendijk, G. A. Steele, H. S. van der Zant and A. Castellanos-Gomez, *Nat. Commun.*, 2014, **5**, 4651.
111. F. N. Xia, H. Wang and Y. C. Jia, *Nat. Commun.*, 2014, **5**, 4458.
112. G. X. Wang, R. Pandey and S. P. Karna, *Nanoscale*, 2015, **7**, 524-531.
113. Y. Li, Y. Zhao, H. H. Cheng, Y. Hu, G. Q. Shi, L. M. Dai and L. T. Qu, *J. Am. Chem. Soc.*, 2012, **134**, 15-18.
114. W. A. Saidi, *J. Phys. Chem. Lett.*, 2013, **4**, 4160-4165.
115. M. Favaro, L. Ferrighi, G. Fazio, L. Colazzo, C. Di Vaentin, C. Durante, F. Sedona, A. Gennaro, S. Agnoli and G. Granozzi, *Acs. Catal.*, 2015, **5**, 129-144.
116. Z. M. Luo, D. L. Yang, G. Q. Qi, J. Z. Shang, H. P. Yang, Y. L. Wang, L. H. Yuwen, T. Yu, W. Huang and L. H. Wang, *J. Mater. Chem. A*, 2014, **2**, 20605-20611.
117. H. L. Fei, R. Q. Ye, G. L. Ye, Y. J. Gong, Z. W. Peng, X. J. Fan, E. L. G. Samuel, P. M. Ajayan and J. M. Tour, *Acs Nano*, 2014, **8**, 10837-10843.
118. L. X. Wang, C. G. Hu, Y. Zhao, Y. Hu, F. Zhao, N. Chen and L. T. Qu, *Carbon*, 2014,

74, 170-179.

119. G. Q. He, Y. Song, K. Liu, A. Walter, S. Chen and S. W. Chen, *Acs Catal.*, 2013, **3**, 831-838.
120. G. Elumalai, H. Noguchi and K. Uosaki, *Phys. Chem. Chem. Phys.*, 2014, **16**, 13755-13761.
121. A. Lyalin, A. Nakayama, K. Uosaki and T. Taketsugu, *Phys. Chem. Chem. Phys.*, 2013, **15**, 2809-2820.
122. T. Y. Wang, J. Q. Zhuo, Y. Chen, K. Z. Du, P. Papakonstantinou, Z. W. Zhu, Y. H. Shao and M. X. Li, *Chemcatchem*, 2014, **6**, 1877-1881.
123. C. C. Du, H. Huang, X. Feng, S. Y. Wu and W. B. Song, *J. Mater. Chem. A*, 2015, **3**, 7616-7622.
124. Y. Zheng, Y. Jiao, Y. H. Zhu, L. H. Li, Y. Han, Y. Chen, A. J. Du, M. Jaroniec and S. Z. Qiao, *Nat. Commun.*, 2014, **5**, 3783.
125. U. Sim, J. Moon, J. An, J. H. Kang, S. E. Jerng, J. Moon, S. P. Cho, B. H. Hong and K. T. Nam, *Energ Environ. Sci.*, 2015, **8**, 1329-1338.
126. D. Y. Pan, C. Xi, Z. Li, L. Wang, Z. W. Chen, B. Luc and M. H. Wu, *J. Mater. Chem. A*, 2013, **1**, 3551-3555.
127. H. Liu, T. Lv, C. K. Zhu, X. Su and Z. F. Zhu, *J. Mol. Catal. a-Chem.*, 2015, **396**, 136-142.
128. W. K. Ho, J. C. Yu, J. Lin, J. G. Yu and P. S. Li, *Langmuir*, 2004, **20**, 5865-5869.
129. H. U. Lee, S. C. Lee, J. G. Won, B. C. Son, S. H. Choi, Y. S. Kim, S. Y. Park, H. S. Kim, Y. C. Lee and J. Lee, *Sci. Rep.-Uk*, 2015, **5**, 8691.
130. X. L. Fu, Y. F. Hu, Y. G. Yang, W. Liu and S. F. Chen, *J. Hazard Mater.*, 2013, **244**, 102-110.
131. C. X. Guo, Y. Q. Dong, H. B. Yang and C. M. Li, *Adv. Energy Mater.*, 2013, **3**, 997-1003.
132. J. Moon, J. An, U. Sim, S. P. Cho, J. H. Kang, C. Chung, J. H. Seo, J. Lee, K. T. Nam and B. H. Hong, *Adv. Mater.*, 2014, **26**, 3501-3505.
133. T. F. Yeh, S. J. Chen and H. S. Teng, *Nano Energy*, 2015, **12**, 476-485.
134. X. X. Li, J. Zhao and J. L. Yang, *Sci. Rep.-Uk*, 2013, **3**, 1858.
135. B. S. Sa, Y. L. Li, J. S. Qi, R. Ahuja and Z. M. Sun, *J. Phys. Chem. C*, 2014, **118**, 26560-26568.
136. G. Z. Sun, J. Q. Liu, X. Zhang, X. W. Wang, H. Li, Y. Yu, W. Huang, H. Zhang and P. Chen, *Angew. Chem. Int. Ed.*, 2014, **53**, 12576-12580.
137. Q. Chen, Y. Zhao, X. K. Huang, N. Chen and L. T. Qu, *J. Mater. Chem. A*, 2015, **3**, 6761-6766.
138. W. W. Liu, Y. Q. Feng, X. B. Yan, J. T. Chen and Q. J. Xue, *Adv. Funct. Mater.*, 2013, **23**, 4111-4122.
139. W. W. Liu, X. B. Yan, J. T. Chen, Y. Q. Feng and Q. J. Xue, *Nanoscale*, 2013, **5**, 6053-6062.
140. Y. Hu, Y. Zhao, G. W. Lu, N. Chen, Z. P. Zhang, H. Li, H. B. Shao and L. T. Qu, *Nanotechnology*, 2013, **24**, 195401.
141. Q. Chen, Y. Hu, C. G. Hu, H. H. Cheng, Z. P. Zhang, H. B. Shao and L. T. Qu, *Phys. Chem. Chem. Phys.*, 2014, **16**, 19307-19313.

142. S. Mondal, U. Rana and S. Malik, *Chem. Commun.*, 2015, **51**, 12365-12368.
143. M. Hassan, E. Haque, K. R. Reddy, A. I. Minett, J. Chen and V. G. Gomes, *Nanoscale*, 2014, **6**, 11988-11994.
144. Y. T. Gong, M. M. Li and Y. Wang, *Chemsuschem*, 2015, **8**, 931-946.
145. P. Wen, P. W. Gong, J. F. Sun, J. Q. Wang and S. R. Yang, *J. Mater. Chem. A*, 2015, **3**, 13874-13883.
146. A. Pakdel, Y. Bando and D. Golberg, *Chem. Soc. Rev.*, 2014, **43**, 934-959.
147. S. Saha, M. Jana, P. Khanra, P. Samanta, H. Koo, N. C. Murmu and T. Kuila, *Acs. Appl. Mater. Inter.*, 2015, **7**, 14211-14222.
148. E. Iyyamperumal, S. Y. Wang and L. M. Dai, *Acs Nano*, 2012, **6**, 5259-5265.
149. Y. Yang, H. L. Fei, G. D. Ruan, C. S. Xiang and J. M. Tour, *Adv. Mater.*, 2014, **26**, 8163-8168.
150. D. L. Chao, C. R. Zhu, X. H. Xia, J. L. Liu, X. Zhang, J. Wang, P. Liang, J. Y. Lin, H. Zhang, Z. X. Shen and H. J. Fan, *Nano Lett.*, 2015, **15**, 565-573.
151. C. R. Zhu, D. L. Chao, J. Sun, I. M. Bacho, Z. X. Fan, C. F. Ng, X. H. Xia, H. Huang, H. Zhang, Z. X. Shen, G. Q. Ding and H. J. Fan, *Adv. Mater. Inter.*, 2015, **2**, 1400499.
152. T. Stephenson, Z. Li, B. Olsen and D. Mitlin, *Energ Environ Sci*, 2014, **7**, 209-231.
153. Y. J. Gong, S. B. Yang, Z. Liu, L. L. Ma, R. Vajtai and P. M. Ajayan, *Adv. Mater.*, 2013, **25**, 3979-3984.
154. C. B. Zhu, X. K. Mu, P. A. van Aken, Y. Yu and J. Maier, *Angew. Chem. Int. Ed.,* 2014, **53**, 2152-2156.
155. H. Pan, *J. Phys. Chem. C*, 2014, **118**, 9318-9323.
156. J. H. Liu, W. F. Li, L. M. Duan, X. Li, L. Ji, Z. B. Geng, K. K. Huang, L. H. Lu, L. S. Zhou, Z. R. Liu, W. Chen, L. W. Liu, S. H. Feng and Y. G. Zhang, *Nano Lett.*, 2015, **15**, 5137-5142.
157. W. F. Li, Y. M. Yang, G. Zhang and Y. W. Zhang, *Nano Lett.*, 2015, **15**, 1691-1697.
158. Q. S. Yao, C. X. Huang, Y. B. Yuan, Y. Z. Liu, S. M. Liu, K. M. Deng and E. J. Kan, *J. Phys. Chem. C*, 2015, **119**, 6923-6928.
159. S. J. Zhao, W. Kang and J. M. Xue, *J. Mater. Chem. A*, 2014, **2**, 19046-19052.
160. J. Sun, H. W. Lee, M. Pasta, H. T. Yuan, G. Y. Zheng, Y. M. Sun, Y. Z. Li and Y. Cui, *Nat. Nanotechnol.*, 2015, **10**, 980-985.
161. P. Gao, K. Ding, Y. Wang, K. Q. Ruan, S. L. Diao, Q. Zhang, B. Q. Sun and J. S. Jie, *J. Phys. Chem. C*, 2014, **118**, 5164-5171.
162. M. Dutta, S. Sarkar, T. Ghosh and D. Basak, *J. Phys. Chem. C*, 2012, **116**, 20127-20131.
163. M. M. Tayakoli, H. Aashuri, A. Simchi, S. Kalytchuk and Z. Y. Fan, *J. Phys. Chem. C*, 2015, **119**, 18886-18895.
164. Y. Li, Y. Hu, Y. Zhao, G. Q. Shi, L. E. Deng, Y. B. Hou and L. T. Qu, *Adv. Mater.*, 2011, **23**, 776-780.
165. J. H. Zhao, L. B. Tang, J. Z. Xiang, R. B. Ji, Y. B. Hu, J. Yuan, J. Zhao, Y. J. Tai and Y. H. Cai, *Rsc Adv.*, 2015, **5**, 29222-29229.
166. V. Gupta, N. Chaudhary, R. Srivastava, G. D. Sharma, R. Bhardwaj and S. Chand, *J. Am. Chem. Soc.*, 2011, **133**, 9960-9963.
167. J. K. Kim, M. J. Park, S. J. Kim, D. H. Wang, S. P. Cho, S. Bae, J. H. Park and B. H.

Hong, *Acs Nano*, 2013, **7**, 7207-7212.

168. J. K. Kim, S. J. Kim, M. J. Park, S. Bae, S. P. Cho, Q. G. Du, D. H. Wang, J. H. Park and B. H. Hong, *Sci. Rep.-Uk*, 2015, **5**, 14276.
169. M. M. Li, W. Ni, B. Kan, X. J. Wan, L. Zhang, Q. Zhang, G. K. Long, Y. Zuo and Y. S. Chen, *Phys. Chem. Chem. Phys.*, 2013, **15**, 18973-18978.
170. Z. C. Ding, Z. Hao, B. Meng, Z. Y. Xie, J. Liu and L. M. Dai, *Nano Energy*, 2015, **15**, 186-192.
171. X. L. Fang, M. Y. Li, K. M. Guo, J. Li, M. C. Pan, L. H. Bai, M. D. Luoshan and X. Z. Zhao, *Electrochim. Acta*, 2014, **137**, 634-638.
172. I. Mihalache, A. Radoi, M. Mihaila, C. Munteanu, A. Marin, M. Danila, M. Kusko and C. Kusko, *Electrochim. Acta*, 2015, **153**, 306-315.
173. E. Lee, J. Ryu and J. Jang, *Chem. Commun.*, 2013, **49**, 9995-9997.
174. L. J. Chen, C. X. Guo, Q. M. Zhang, Y. L. Lei, J. L. Xie, S. J. Ee, G. H. Guai, Q. L. Song and C. M. Li, *Acs. Appl. Mater. Inter.*, 2013, **5**, 2047-2052.
175. Z. L. Zhu, J. A. Ma, Z. L. Wang, C. Mu, Z. T. Fan, L. L. Du, Y. Bai, L. Z. Fan, H. Yan, D. L. Phillips and S. H. Yang, *J. Am. Chem. Soc.*, 2014, **136**, 3760-3763.
176. J. Dai and X. C. Zeng, *J. Phys. Chem. Lett.*, 2014, **5**, 1289-1293.
177. Y. X. Deng, Z. Luo, N. J. Conrad, H. Liu, Y. J. Gong, S. Najmaei, P. M. Ajayan, J. Lou, X. F. Xu and P. D. Ye, *Acs Nano*, 2014, **8**, 8292-8299.
178. Y. B. Song, S. J. Zhu and B. Yang, *Rsc Adv.*, 2014, **4**, 27184-27200.
179. Z. T. Fan, S. H. Li, F. L. Yuan and L. Z. Fan, *Rsc Adv.*, 2015, **5**, 19773-19789.
180. X. T. Zheng, A. Than, A. Ananthanaraya, D. H. Kim and P. Chen, *Acs Nano*, 2013, **7**, 6278-6286.
181. Y. H. Xu, J. Q. Liu, C. L. Gao and E. K. Wang, *Electrochem. Commun.*, 2014, **48**, 151-154.
182. N. Li, X. W. Wang, J. Chen, L. Sun and P. Chen, *2D Mater.*, 2015, **2**, 034018.
183. K. Hola, Y. Zhang, Y. Wang, E. P. Giannelis, R. Zboril and A. L. Rogach, *Nano Today*, 2014, **9**, 590-603.
184. S. H. Song, M. H. Jang, J. Chung, S. H. Jin, B. H. Kim, S. H. Hur, S. Yoo, Y. H. Cho and S. Jeon, *Adv. Opt. Mater.*, 2014, **2**, 1016-1023.
185. S. Balendhran, S. Walia, H. Nili, S. Sriram and M. Bhaskaran, *Small*, 2015, **11**, 640-652.
186. E. Bianco, S. Butler, S. S. Jiang, O. D. Restrepo, W. Windl and J. E. Goldberger, *Acs Nano*, 2013, **7**, 4414-4421.
187. M. Naguib, V. N. Mochalin, M. W. Barsoum and Y. Gogotsi, *Adv. Mater.*, 2014, **26**, 992-1005.
188. L. T. Dou, A. B. Wong, Y. Yu, M. L. Lai, N. Kornienko, S. W. Eaton, A. Fu, C. G. Bischak, J. Ma, T. N. Ding, N. S. Ginsberg, L. W. Wang, A. P. Alivisatos and P. D. Yang, *Science*, 2015, **349**, 1518-1521.
189. W. Jaegermann and D. Schmeisser, *Surf. Sci.*, 1986, **165**, 143-160.
190. X. Y. Chia, A. Y. S. Eng, A. Ambrosi, S. M. Tan and M. Pumera, *Chem. Rev.*, 2015, **115**, 11941-11966.